

Lavran Thorstensen

Welding and Mechanical Testing of Aluminium Alloys for use in Constructions

Master's thesis in Material Science and Engineering

Supervisor: Trond Furu

Co-supervisor: Ole Runar Myhr and Bjørn Holmedal

June 2023

Lavran Thorstensen

Welding and Mechanical Testing of Aluminium Alloys for use in Constructions

Master's thesis in Material Science and Engineering
Supervisor: Trond Furu
Co-supervisor: Ole Runar Myhr and Bjørn Holmedal
June 2023

Norwegian University of Science and Technology
Faculty of Natural Sciences
Department of Materials Science and Engineering



Preface and Acknowledgements

This master thesis was carried out at the Department of Material Science and Engineering at the Norwegian University and Technology (NTNU), in collaboration between Norsk Hydro, SINTEF Industry and SINTEF Manufacturing.

I would like to use this moment to thank my main supervisor Trond Furu, as well as my co-supervisors Bjørn Holmedal and Ole-Runar Myhr, for their thorough commitment and close guidance in this project. I would also like to thank the chief engineers Pål Christian Skaret, Berit Vinje Kramer, Dmitry Slizovskiy and Marit Elinda Olaisen Odden, as well as phd. candidate Ruben Åge Hansen, for their assistance in the experimental part of this project. In addition, I would like to thank SINTEF Manufacturing for allowing allowing me to use friction stir welding (FSW) situated at Raufoss, and especially Siri Marthe Arbo and Per Paulsen who assisted during the FSW experiments at SINTEF Manufacturing. SINTEF Industry situated in Trondheim also deserves appreciation for all the help with conducting MIG welding experiments. Morten Høgseth Danielsen and Nikolai Marhaug helped planing and carrying out the MIG welding and sample preparation. Lastly, I would like to thank senior scientist Bård Nyhus at SINTEF Industry for all the help with coordinating the MIG experiments, as well as providing the plates used in this thesis.

Abstract

The aim of this thesis is to produce Al-Si-Mg alloys to be used in large constructions, while having a small strength decrease from welding. Different cooling methods from solution heat treatment have been investigated and compared to similar alloys that is commonly used in large constructions today. What was found, is that cooling metal plates in warm water has the most promising mechanical properties. It is assumed that this cooling method works best because of a larger concentration of β'' particles that contribute to a high strength in Al-Si-Mg alloys. In addition it was found that FSW seems to be a better welding option for the aim of this thesis than metal inert gas (MIG). Lastly, the results have been compared to the simulation model NaMo. This model calculated the hardness in the base material with an error of only 6%, but struggled more with giving accurate predictions closer to the weld, and to describe the tensile strength of the metal.

Sammendrag

Målet med denne masteroppgaven er å produsere Al-Si-Mg legeringer til bruk i store konstruksjoner, samtidig som styrken ikke skal bli redusert i noen særlig grad som følge av sveising. Metallplater har gått gjennom ulike nedkjølingmetoder etter innherding, og mekaniske egenskaper har blitt sammenlikna med plater som har opplevd et temperaturforløp som vanligvis brukes i dag. Det viste seg at å kjøle platene i varmt vann ga de beste resultatene. Det antas at kjøling i varmt vann gir bedre mekaniske egenskaper ettersom det bør gi større konsentrasjoner av β'' partikler som har et stort styrkebidrag i Al-Si-Mg legeringer. I tillegg viste det seg at friksjonssveising virker å være en bedre sveisemetode for målet med denne masteroppgaven enn metal inert gass sveising. Til slutt har resultatene blitt sammenlikna med simuleringsmodellen NaMo. Denne modellen hadde en feil i hardhet til basematerialet på kun 6%, men slet mer med nøyaktige beregninger nærmere sveisen, og med å beskrive strekkfastheten til metallet.

Table of Contents

Preface	ii
Abstract	iii
Sammendrag	iv
List of Figures	v
List of Tables	vii
List of Abbreviations	ix
1 Introduction	1
1.1 Background and Motivation	1
1.2 Aim and Scope	1
2 Theory	2
2.1 The Al-Si-Mg alloy	2
2.2 The Precipitates in Al-Si-Mg alloys	2
2.2.1 Precipitation Hardening	2
2.2.2 Precipitation sequence of the Al-Si-Mg alloy	4
2.3 Welding of Al alloys	7
2.3.1 Metal Inert Gas Welding	8
2.3.2 Fusion Weld zones	9
2.3.3 Friction Stir Welding	11
2.3.4 Friction Stir Weld Zones	12
2.4 The relation between Engineering Stress and Strain, and True Stress and Strain . .	13
2.5 Simulation of the temperature development for medium thick plates	14
2.6 Simulation of precipitation, work hardening and strength for Al-Si-Mg alloys . . .	16
2.6.1 Precipitation model	17
2.6.2 Strength model	22
2.6.3 Overall hardness and yield strength	22
2.6.4 Work hardening model	23
2.6.5 Solid solution hardening	24
2.6.6 Yield stress model	25
3 Experimental	26

3.1	Chemical Composition	26
3.2	Plate preparation, Heating and Cooling	26
3.3	Friction Stir Welding	28
3.3.1	Welding parameters	28
3.3.2	Welding tool	29
3.4	Metal Inert Gas Welding	30
3.5	Material Characterization	31
3.5.1	Grinding and Polishing	31
3.5.2	Optical Microscopy and Hardness Measurements	32
3.6	Conductivity Measurements	32
3.7	Tensile Testing	33
4	Results	36
4.1	Grain structure	36
4.2	Hardness	40
4.3	Conductivity	42
4.4	Tensile test	45
5	Discussion	49
5.1	The Microstructure in the Base Material	49
5.2	Properties of the Weld Zones	50
5.3	The Preciseness of the NaMo model	51
5.4	Which Cooling Method and Welding Technique is the Best?	52
6	Conclusions	53
7	Further Work	54
	References	55
	Appendix	59
	A Temperature Measurements During Welding	59
	B Inputs NaMo	64
 List of Figures		
1	How the critical radius is for the transition between particle shearing and Orowan bowing. critical resolved shear stress [40].	2

2	How dislocations interact with an array of point obstacles [40].	3
3	(a) shows how a dislocation can bulge between particles, while (b) illustrates how a dislocation loops around particles after the dislocation have passed [40].	4
4	The manufacturing process used for extruded Al-Si-Mg alloys [65].	4
5	The left side of the phase diagram for Al-Si-Mg alloys [14].	5
6	How the strength of Mg rich Al-Si-Mg alloys develop with aging time [24].	7
7	A sketch of the gas metal arc welding (GMAW) process [41].	8
8	How the power tops in the SyncroPulse method is. The high power tops can vary from 10% to 90%, and the frequency, F , can be between 0.5 to 3.0 Hz [69].	9
9	An illustration of the different zones in a fusion welded plate [26].	10
10	The solidification structure in fusion welds [25].	10
11	The strength in the HAZ, shown for three cases: immediately after fusion welding, after NA and after AA [25].	11
12	The relationship between process parameters and different defects. The region called Sound Joints is where the good welds are obtained. The figure is taken from [3].	12
13	The profile of the cross section of a FSW alloy [36].	13
14	Illustration of the medium thick plate solution, showing real and imaginary point sources on a medium thick plate [34].	15
15	How the isotherm lines look for a cross section of an aluminium weld. The figure is taken from [34].	16
16	The different submodels in NaMo, showing what was unchanged, modified or new in 2018 [56].	17
17	The dimensions of each plate, as well as the position of the hole	26
18	The temperature in the plates during cooling from 430°C	27
19	The temperature in the plates during cooling from 550°C	27
20	The X-shaped surface on the plates prepared for MIG welding. As can be seen in the figure, the angle was 60°.	28
21	The position of all thermoelements used for FSW. The text in the figure tell the distance of the thermoelement from the weld centre	28
22	A picture of the welding tool used in the friction stir welding experiments.	30
23	The position of all thermoelements used for MIG welding. The text in the figure tell the distance of the thermoelement from the weld centre.	31
24	A picture of the Sigmatest 2.069.	33
25	A picture of the tensile testing process.	34
26	The dimensions of the specimens used in tensile testing.	34
27	The grain structure of the FSW plate heated to 430°C and cooled in the oven.	37
28	The grain structure of the MIG welded plate heated to 550°C and cooled in warm water.	38
29	The grain structure of the FSW plates.	39

30	The grain structure of the MIG welded plates.	40
31	The hardness of all the FSW plates	41
32	The hardness of all the MIG plates heated to 430°C	41
33	The hardness of all the MIG plates heated to 550°C	42
34	The conductivity of all the FSW plates heated to 430°C.	43
35	The conductivity of all the MIG plates heated to 430°C.	44
36	The conductivity of all the MIG plates heated to 550°C.	45
37	The conductivity of all the MIG plates heated to 550°C.	46
38	The conductivity of all the MIG plates heated to 550°C.	47
39	The conductivity of all the MIG plates heated to 550°C.	48
40	The temperature during FSW of the T6-reference alloy. The temperature was measured at the distances 5mm, 9mm and 13mm from the weld centre, as can be seen in the figure.	59
41	The temperature during FSW of the warm water cooled alloy after heating to 430°C. The temperature was measured at the distances 5mm, 9mm and 13mm from the weld centre, as can be seen in the figure.	60
42	The temperature during MIG welding of the alloy cooled in the oven after heating to 430°C for the first weld. The temperature was measured at the distances 5mm, 9mm and 13mm, 25mm and 75mm from the weld centre, as can be seen in the figure.	61
43	The temperature during MIG welding of the alloy cooled in the oven after heating to 430°C for the second weld. The temperature was measured at the distances 5mm, 9mm and 13mm, 25mm and 75mm from the weld centre, as can be seen in the figure.	62
44	The temperature during MIG welding of the air cooled alloy after heating to 550°C for the first weld. The temperature was measured at the distances 5mm, 9mm and 13mm from the weld centre, as can be seen in the figure.	63
45	The temperature during MIG welding of the air cooled alloy after heating to 550°C for the second weld. The temperature was measured at the distances 5mm, 9mm and 13mm from the weld centre, as can be seen in the figure.	64
46	The input to NaMo at a distance 9mm from the weld centre for the plate in a T6 reference state experiencing FSW.	65
47	The input to NaMo at a distance 9mm from the weld centre for the warm water cooled plate experiencing FSW.	66
48	The input to NaMo at a distance 9mm from the weld centre for the plate cooled in the oven experiencing MIG welding after being heated to 430°C.	67
49	The input to NaMo at a distance 9mm from the weld centre for the air cooled plate experiencing MIG welding after being heated to 550°C.	68

List of Tables

1	Expressions for the different nucleation laws implemented in the NaMo model [55].	19
2	Expressions for the different growth laws implemented in the NaMo model [55]. . .	20

3	The chemical composition of the Al-Si-Mg alloy investigated in this thesis. All the values are given in wt%.	26
4	Welding parameters used in the FSW experiments.	29
5	Information about the welding tool used in the friction stir welding experiments. Information is given about both the pin and the shoulder.	29
6	Welding parameters used in the MIG experiments. All parameters were kept the same for both welding except the current, which were 165A for the first weld and 185A for the second.	31
7	The grinding and polishing steps.	32
8	The most likely microstructure in the base material for each cooling method after heating to 430°C	49
9	The most likely microstructure in the base material for each cooling method after heating to 550°C	49

Abbreviations

AA artificial aging

APT atom probe tomography

CMT cold metal transfer

DSC differential scanning calorimetry

FSW friction stir welding

FZ fusion zone

GMAW gas metal arc welding

GP-zones Guiner-Preston zones

HAZ heat affected zone

HV Vicker's hardness

MIG metal inert gas

NA natural aging

NaMo nanostructure model

PALS positron lifetime annihilation spectroscopy

PFZ precipitate-free zone

PWHT post weld heat treatment

SHT solution heat treated

SSSS supersaturated solid solution

SZ stir zone

TEM transmission electron microscope

TMAZ thermomechanically affected zone

WTCP weld thermal cycle program

1 Introduction

1.1 Background and Motivation

In large constructions it is often important to use materials with great mechanical properties in addition to a low cost and a low weight. A material that meets these requirements is the metal aluminium. Different aluminium alloys have different properties, but for large constructions the Al-Si-Mg alloy is commonly used because of the high yield strength. A popular type of the Al-Si-Mg alloy, is the AA-6082 alloy.

As it is for all metals, the mechanical properties of an Al-Si-Mg alloy depends on the microstructure. For this metal, the dominating strength contribution comes from the precipitate hardening, resulting from heat treatment. This means that in order to get great mechanical properties it is necessary to do a sensible thermodynamical processing in addition to picking the correct alloy.

A good understanding of how a high strength is reached for Al-Si-Mg alloys has already been obtained. This is done by keeping the metal at a high temperature for some hours. What is more complicated is when welding also is included in the process. Welding leads to high temperatures locally, changing the microstructure and often reducing the strength. This means that large constructions tend to be made of a high strength alloy with some local weaknesses, leading to these local weaknesses being what the constructions must be dimensioned after. Often this is solved by applying some extra material near the weld, by increasing the strength by some clever geometry or by some similar local strength adding measure.

1.2 Aim and Scope

The point of this thesis is to optimize production of Al-Si-Mg alloys for large constructions, by proposing a different heat treatment than what is common today. This is based on the question of the point of having a high strength material, if the point around the weld ends up much weaker anyway. Could it be that age hardening of Al-Si-Mg alloys is unnecessary, and that time and money could be saved if this processing step is skipped? Could it also be possible to avoid quenching since this can deform structures, and implement slower cooling times from the solution heat treatment temperature? Could this be a better option than having a local strength increase near the weld? Is this alternative processing method more sustainable?

The way all the questions for this thesis is answered is by considering three different cooling rates and two different welding techniques, and comparing these to reference alloys of the high strength T6 state. There has been made an effort of finding good welding parameters for these processes, and avoid common welding defects. All the different experiments have been documented by photography in light optical microscope near the weld and in the base material, and hardness tests have been taken over the same area. In addition, tensile testing has been done across the weld. This gives a good understanding of the mechanical properties of the alloy, and the connection to thermal processing.

Lastly, it should be mentioned that the simulation tool called the NaMo model has been compared to all experimental results. This is a model developed by Hydro over nearly two decades, with the power of predicting both the microstructure and the mechanical properties of Al-Si-Mg alloys based on the thermal history of the metal. The point of this is to either validate if the model is correct or to identify any rooms for improvement, as the model has not been tested against similar heat treatments before. If this model proves accurate, one possibility is to run this model until the "perfect" heat treatment is found, and later verify this experimentally. This would then be a much faster, easier and cheaper alternative than testing a lot of parameters on the lab.

A more detailed description of the Al-Si-Mg alloy and how heat treatment and precipitation hardening works is given in section 2. Here the main equations and assumptions NaMo model is also explained.

2 Theory

2.1 The Al-Si-Mg alloy

Al-Si-Mg alloys are aluminium alloys with silicon (Si) and magnesium (Mg) as the main alloying elements. These alloys are called the 6xxx series of aluminium. The Mg and Si concentrations have a range between 0.5-1.3 wt% and 0.4-1.4 wt% respectively [23]. These alloying elements makes it possible to precipitate particles in the alloys through thermomechanical processing, and these particles contribute for about 70% of strength of the alloys. What characterises the Al-Si-Mg alloys is a moderate strength, good weldability, good machinability and good formability [11].

2.2 The Precipitates in Al-Si-Mg alloys

The main strength contribution in Al-Si-Mg alloys come from the precipitates [9]. These precipitates are made from the Si and Mg alloying elements. So to get a metal with desired mechanical properties, it is necessary to understand the precipitation sequence for the Si-Mg particles. Today this understanding exists, and is used to produce high strength Al-Si-Mg alloys. The state of maximum strength obtainable is called the T6 state [59], and this is what is normally obtained through production. This subsection focuses on presenting the processing steps before explaining the precipitation sequence and which precipitates contribute to the most strength, and how the T6 state is obtained. In addition, information is given about how precipitates in general will interact with dislocations increasing the yield strength of metals.

2.2.1 Precipitation Hardening

When a material is subjected to stress exceeding the yield strength, dislocations will move. This movement of dislocations leads to plastic deformation, meaning that in order to gain a hard material the dislocation movement must be prevented. Precipitates will take this role. There are two ways precipitates can prevent dislocation movement, and this is either by having dislocations shearing through them or having to bow around them. Which of these happen is determined by the precipitate size. This transition is illustrated in figure 1. It should be noted that when dislocations bow around precipitates this is called Orowan bowing. Another note is that plastic deformation will increase the yield strength of metals [9].

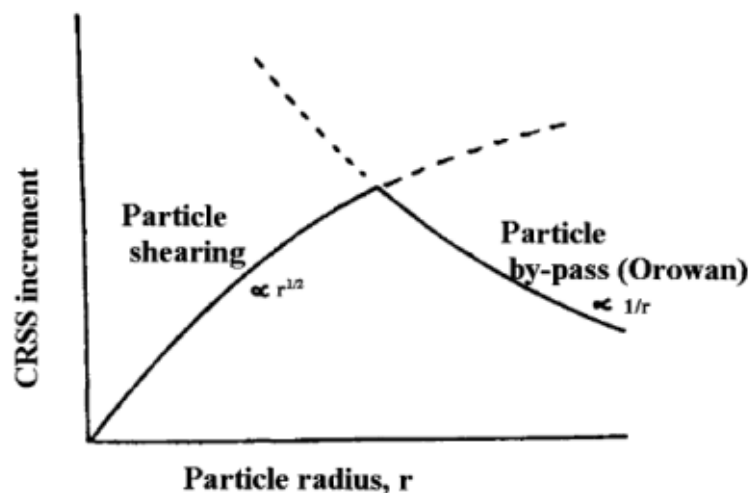


Figure 1: How the critical radius is for the transition between particle shearing and Orowan bowing. critical resolved shear stress [40].

For a metal full of precipitates, it is possible to express mathematically how the dislocations will interact with them. This is achieved by assuming that the precipitates are points of identical strength within the matrix [9]. Figure 2 shows a physical representation of this interaction.

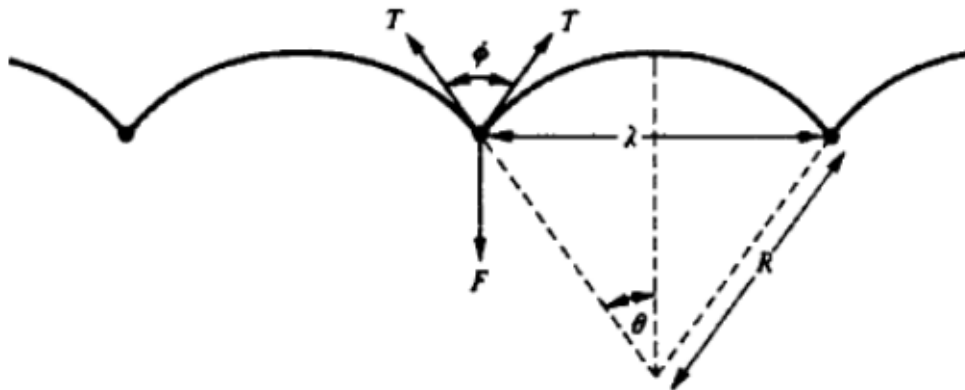


Figure 2: How dislocations interact with an array of point obstacles [40].

In figure 2, F , is the force necessary to shear through the particle, T is the dislocation line tension, ϕ is the breaking angle, R is the radius of curvature and λ is the interparticle distance. It is possible to express the force as [40],

$$F = 2T \cos\left(\frac{1}{2}\phi\right). \quad (1)$$

For a the beaking angle, ϕ , equal zero, the precipitate acts as an impenetrable object, but for all breaking angles above zero, the particle is shearable [40]. For shearable particles, there are several mechanisms in that the precipitate contribute to preventing dislocation movement. One of these is the chemical strengthening due to formation of additional particle matrix interface [40].

When the breaking angle is zero the particle is unshearable, which cases the bulging dislocation to eventually interact with itself and annihilate. This will eventually result in a dislocation loop surrounding the particle after the passing of the dislocation [9]. This concept is illustrated in figure 3.

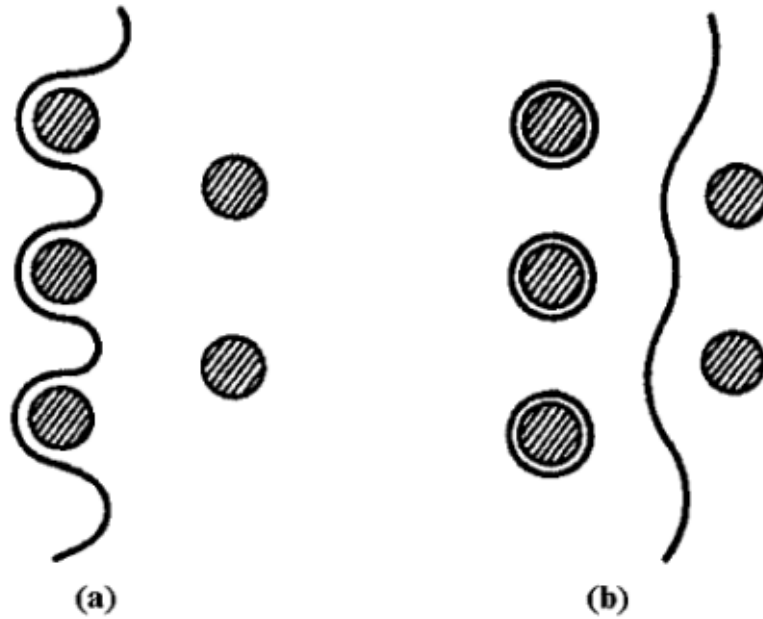


Figure 3: (a) shows how a dislocation can bulge between particles, while (b) illustrates how a dislocation loops around particles after the dislocation have passed [40].

2.2.2 Precipitation sequence of the Al-Si-Mg alloy

For extruded profiles of the Al-Si-Mg alloy the processing steps include casting, homogenization, preheating, extrusion, cooling and aging. This is shown in figure 4.

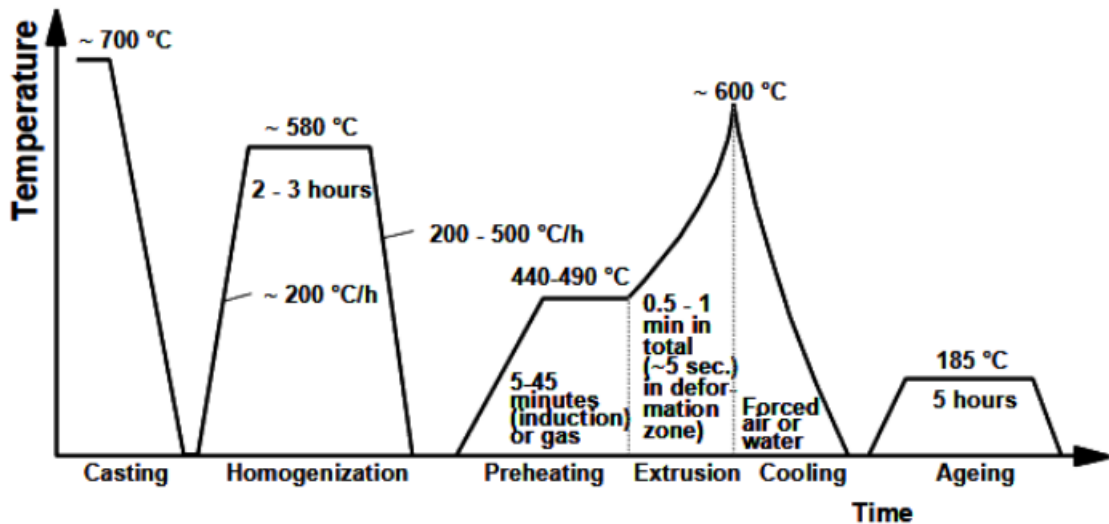
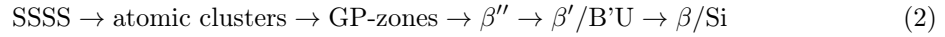


Figure 4: The manufacturing process used for extruded Al-Si-Mg alloys [65].

The first steps of this processing will not affect the precipitation sequence. This is because high temperatures will "reset" the microstructure, meaning that the properties of the alloy is determined from the extrusion and following aging. The precipitation sequence that happens during these steps are summarized in equation 2 [39].



As can be seen in equation 2, the first step of the precipitation sequence is the formation of a supersaturated solid solution (SSSS). This is when all alloying elements become solved in the Al matrix at room temperature, and it is obtained through solution heat treated (SHT) followed by quenching. SHT is a processing step where the metal is heated at temperatures above the solvus temperature. This treatment will last until all Si and Mg atoms are solved in the Al matrix and the basis for a SSSS is made. In addition to having all alloying elements solved in the Al matrix, the SSSS also consists of a lot of vacancies. Quenching will preserve this microstructure to room temperature [66].

To form a SSSS the Al-Si-Mg alloy must have a Mg_2Si content below 1.85 wt%. This can be seen from the phase diagram given in figure 5 [14]. The phase diagram also shows that the temperature of SHT should be below 595°C to avoid local melting [66]. Normal SHT temperatures for Al-Si-Mg alloys range from 535 to 575°C [59].

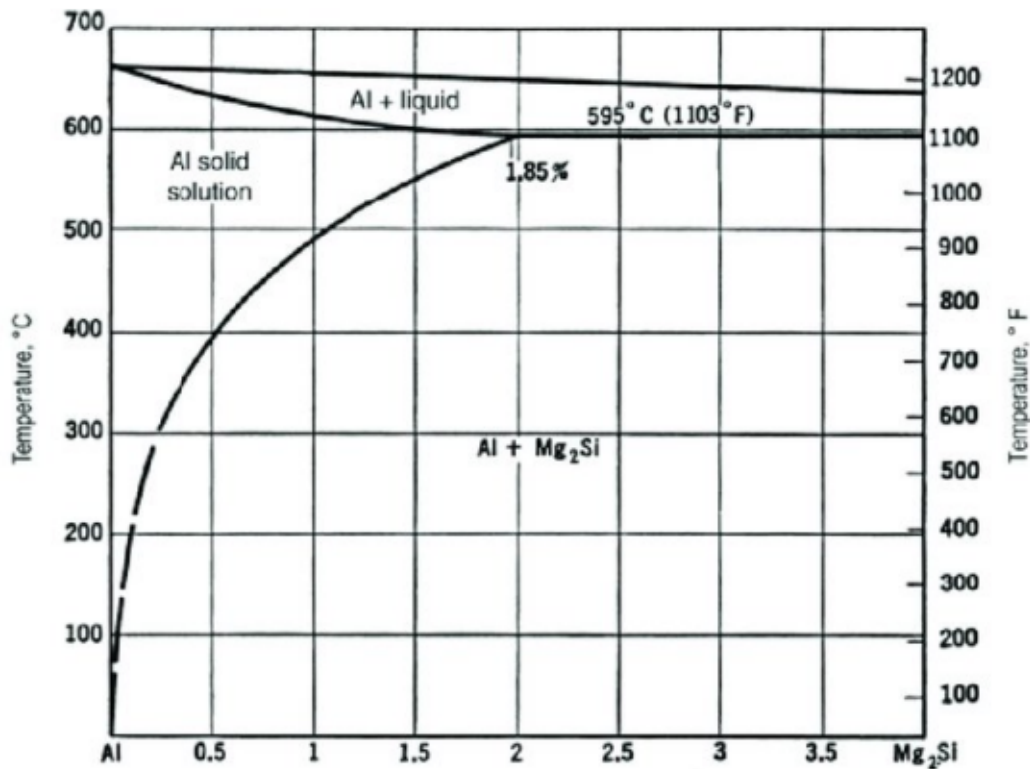


Figure 5: The left side of the phase diagram for Al-Si-Mg alloys [14].

The initial stage of age hardening considers a structure right after quenching. This structure consists of clusters of solute atoms and vacancies, and is hard to study. atom probe tomography (APT) and other visualizing characterization methods cannot be done, due to the meticulous and time consuming sample preparation [10]. This means that characterization methods of a more indirect nature requiring less sample preparation time must be used. Two such methods are differential scanning calorimetry (DSC) and positron lifetime annihilation spectroscopy (PALS). These are often employed to study the onset of ageing [15, 35].

Banhart *et al.* found that solute Si is believed to accompany vacancies after quenching in pure ternary Al-Si-Mg alloys using PALS [6]. This is backed up by reportings from Edwards *et al.* [15], who suggests that individual clustering of solute Si and Mg occur immediately after quenching based on DSC analysis. Edwards *et al.* also suggests that vacancies are accompanying Si clusters,

similar to what happens after quenching binary Al-Si alloys. They mean that Mg clusters eventually dissolve and act as feeding material for growing co-clusters.

When it comes to the onset of NA, investigations with PALS were done by Liu *et al.* [35]. The group proposed a growth mechanism where vacancies tied to solute-vacancy clusters migrate towards solute atoms. Later these atoms diffuse and bind to the solute vacancy clusters, creating vacancy free co-clusters of Mg and Si. Still, Liu *et al.* point out that there still is a lot of uncertainty about these early phenomena even though some research has been done.

In the early stages of aging several types of co-clusters may form. Some of these acts as nuclei for strengthening particles, while other do not. Marioara *et al.* showed that heat treating Al-Si-Mg alloys at temperatures of 125 or 150°C immediately after quenching to RT improves the precipitation hardening of strengthening β'' particles [38]. Storing the material a while at room temperature, for later heat treating it at 125 or 150°C, on the other hand, yields a softer material according to Murayama *et al.* [48]. The group claims that the co-clusters arising during NA are smaller than the required size to survive at elevated temperatures, leading to dissolution during AA. Furthermore, precipitation kinetics after reversion of these clusters will decline because of vacancies annealing at the high temperatures. This will continue until the equilibrium vacancy concentration is reached. Marioara *et al.* report that a density of GP-zones sometimes ends up five times less in the material that was stored at room temperature, compared to the material experiencing heat treatment immediately after quenching.

Investigations of the clustering behaviour of Al-Si-Mg alloys during both NA and heat treatment immediately after quenching were conducted by Torsæter *et al.* [74]. They studied two different Al-Si-Mg alloys, one with a total wt% of Si and Mg less than 1%, and one where the total wt% of Si and Mg were above 1%. Their research showed that high amounts of clusters with a Si/Mg ratio close to 1 were formed during heating right after quenching. After some time, these clusters become GP-zones. During NA different results were obtained. For the alloy with a total Si and Mg content below 1%, the same clusters were found, but in significantly lower concentrations. When the solute content was above 1%, a high concentration of clusters with a Si/Mg ratio different to 1 formed. These clusters were high in either Si or Mg content, and had a negative impact on GP-zone formation. Fallah *et al.* have shown that clusters acting as precursors for GP-zones are spherical with a fcc crystal structure [16].

According to equation 2, the co-clusters will eventually evolve into structures named Guiner-Preston zones (GP-zones). These structures have a high coherency with the fcc structure of the former clusters, even though they have another structure themselves [16]. Many different morphologies of the GP-zones are found in the literature. Some have reported a spherical structure [77, 49], while others think GP-zones are needle like shaped [37]. Hastings *et al.* explain how various GP-zones may form depending on the chemical composition of the Al-Si-Mg alloy [27]. Research by Matsuda *et al.* indicates that Mg rich Al-Si-Mg alloys will give plate shaped GP-zones [42]. Experiments conducted by Marioara *et al.*, indicate that Mg rich environments will suppress the GP-zone type precipitating β'' particles [39]. This GP-zone is called pre- β'' type GP-zone.

When it comes to the β'' particles, these are semi coherent and needle shaped with a monoclinic crystal structure growing in the $\langle 100 \rangle$ directions [77]. Furthermore Marioara *et al.* show that the chemical composition of the β'' particles are Mg_5Si_6 [77]. However, other studies conducted in 2009 indicate that a chemical composition of $Mg_5Al_2Si_4$ may actually be the correct one [27].

As briefly explained before, the β' particle will form from the β'' particle. β' particles have a hexagonal structure, with a Mg-Si ratio close to 1.7 [77]. They also are less coherent in the Al-matrix than β'' particles.

Instead of the β' particle, the U - and B'-phases may form from the β'' particle. The U-phases can be found where the Si/Mg ratio is above 1.1, and they are split into two parts: U1 and U2 [39]. The U2 phase seems more common than the U1 phase. Another particle is the B' particle, which is a lath shaped particle with unknown composition. Neither the U or B' phases give a large contribution to the strength of Al-Si-Mg alloys, and will therefore not be described any further.

The final and largest particles to form in the precipitation sequence are the β particles and the Si

plates. β particles are incoherent and plate shaped particles, with a chemical composition given as Mg_2Si [77]. A study by Marioara *et al.* showed that Si plates were only found in Al-Si-Mg alloys with a high Si/Mg ratio [39]. The β particles are thermodynamical stable at room temperature, and is therefore called the equilibrium phase.

Marioara *et al.* investigated the strength contribution from each of the different particles, as well as the connection between alloy composition and strength giving particles. What they found was that the most strength contribution came from β'' particles and GP-zones, where the β'' had the largest contribution. In addition, the concentration of these strength contributing particles were at the highest in the Si rich regions. During aging at 175°C, a hardness peak was observed twice. The first came at 3h, while the second showed up after 17h. Peak number one was from the GP-zones, while the higher second came from the β'' particles. When a similar experiment were conducted for a Mg rich alloy only one peak were found, resulting from the β'' particles. The group also found that β'' and β' particles are present simultaneously in Mg rich alloys. The alloy with the most strength had an alloying element composition close to Mg_5Si_6 [39]. The strength development with aging time for Mg rich Al-Si-Mg alloys is presented in figure 6.

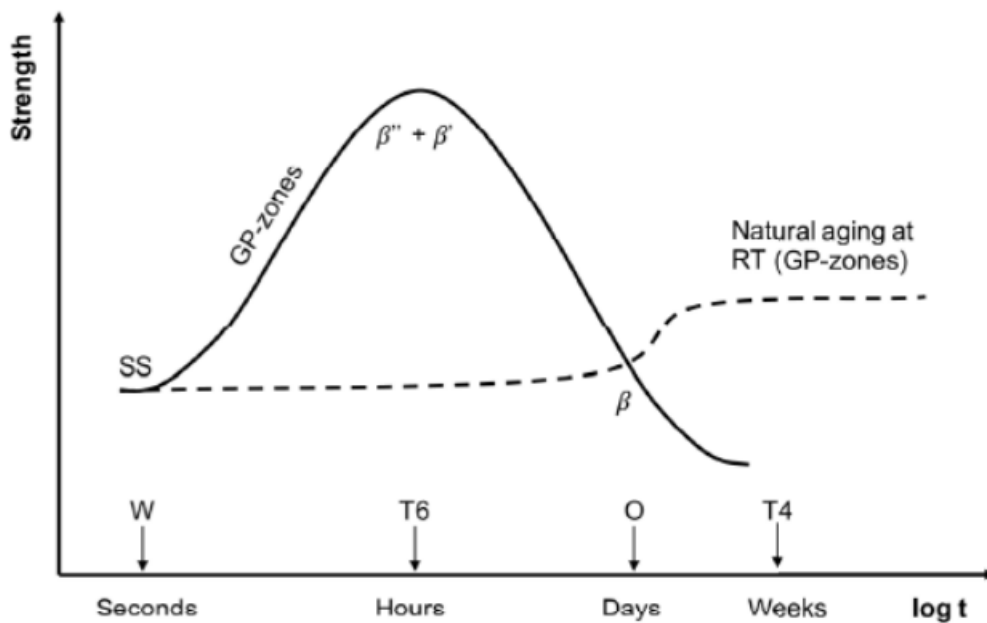


Figure 6: How the strength of Mg rich Al-Si-Mg alloys develop with aging time [24].

From figure 6, it is clear that two different strengthening processes can happen during aging. These are artificial aging (AA) and natural aging (NA). AA happens at temperatures between 150 and 200°C, and this is what is illustrated in figure 4. This process leads to the maximum strength T6 state for the alloy due to formation of β'' particles. It can be seen in figure 6 that this strength is significantly higher than the strength at other times. A common AA temperature and time for Al-Si-Mg alloys is 185°C for 5.5 h [59]. Further heat treatment of an Al-Si-Mg alloy in the T6 state will decrease the material strength, and the metal becomes overaged. NA is aging at room temperature. This both leads to a lower strength and takes longer time, as can be seen in figure 6.

2.3 Welding of Al alloys

In this thesis two different welding techniques are used. These are MIG and FSW. In this subsection both these welding techniques are described, as well as their influence on the metal and the properties arising close to the weld. Lastly, these welding techniques are compared by cost, sustainability and mechanical properties of the welded Al alloys.

2.3.1 Metal Inert Gas Welding

MIG welding is a type of gas metal arc welding (GMAW). GMAW processes are traditional welding methods. A sketch of the GMAW process is given in figure 7.

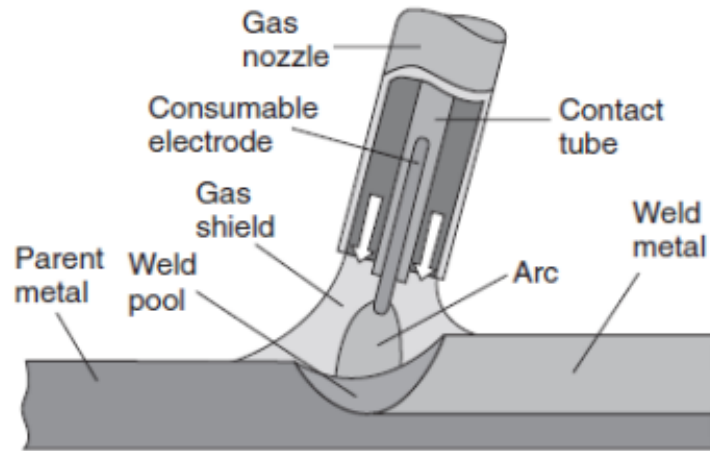


Figure 7: A sketch of the GMAW process [41].

All GMAW processes utilize gas and wire feeding. An electric current is directed via the wire from the welding machine through the workpiece, before looping back to the machine through a cable attached to the workpiece. This makes a closed loop. An arc is struck between the wire tip and the workpiece during welding, melting both the wire and the metal workpiece. Because of this, constant feeding of the wire is necessary to maintain an arc. Another consequence is that the wire is being utilized as filler material in the weld. Recommended filler wire materials for MIG welding Al-Si-Mg alloys are AA5356, AA5183 and AA4043 [44]. The shielding gas used in the process is often a mixture of argon (Ar) and helium (He). The gas engulfs the weld pool, preventing ambient oxygen from oxidizing the molten metal.

The GMAW machine can be used with a high voltage and current. If this is the case, transportation of the filler wire to the work piece is done through a spray arc process. Melting of filler material is done by the arc, and the filler material is later transferred to the work piece as small droplets. Since high voltage and ampere is used, this welding process has a high heat input. It should also be mentioned that the filler wire never contacts the weld pool with this setting [79].

When using a low voltage and current on the GMAW machine, the deposition of the filler material to the weld is done by something called short arc welding. In this process, the tip of the filler wire melts forming a drop of molten metal. As suggested by the name, a short arc weld length is required. This allows contact between the weld pool and the metal drop which is attached to the filler wire. This process repeats itself 200 times per second [79, 80]. Unstable arcs may occur for short arc welding, meaning that spatter during welding can occur [80]. This is a low heat input welding process since the applied voltage and current is low.

As an alternative to short arc welding, pulse MIG welding has been developed. This type of MIG welding employs a power source with ability to apply the power in pulses. These pulses may vary from 30 to 300 Hz, with a power cycling between high and low values. Drops of molten metal from the filler wire will pinch off at the same rate as the wire is fed as a result of the pulsations. This prevents the problem found in short arc welding with short circuiting and spatter when the filler wire connects with the weld pool [79, 80]. The combination of a low heat input and no spatter makes pulse MIG welding a great choice for welding of aluminium [80]. Another advantage with the method is that pulse MIG transmission is able to weld thin materials (1-4mm thick). This is better than ordinary MIG, which usually only welds materials of a thickness of 3-20mm. [5]

The equipment manufacturer Fronius International GmbH has developed another MIG welding method called SynchroPulse. This method uses a welding power that cycles between a low and a high power state. The duration of the high power tops can be adjusted, resulting in a low heat input and little spatter. The welding power and the wire feed speed must be changed accordingly [69]. Figure 8 shows the SynchroPulse concept.

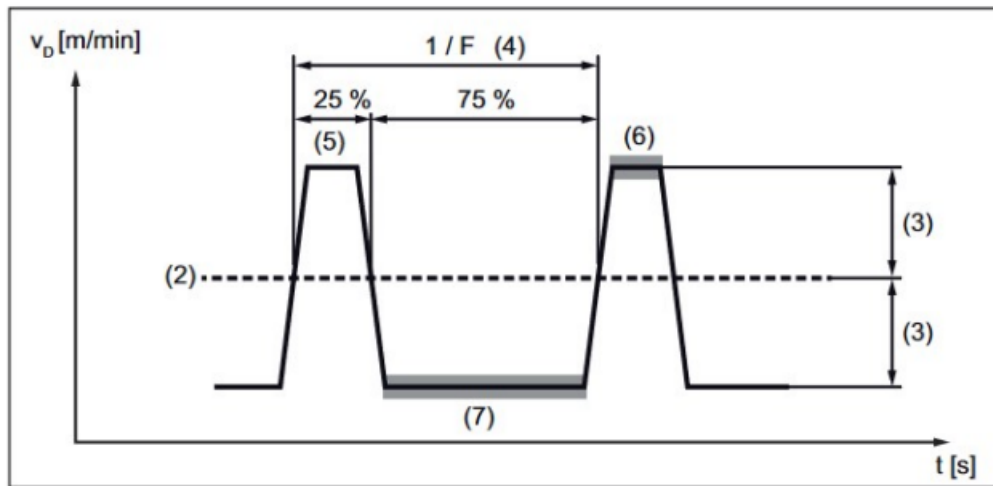


Figure 8: How the power tops in the SynchroPulse method is. The high power tops can vary from 10% to 90%, and the frequency, F , can be between 0.5 to 3.0 Hz [69].

A different MIG welding method based on conventional short arc welding is cold metal transfer (CMT). In CMT, the filler wire is retracted once it comes in contact with the weld pool. Then the welding current approaches zero, which prevents spattering of molten metal. After the metal is deposited and the filler wire is retracted, the process repeats. This can happen up to 70 times per second. As the welding current approaches zero, the same happens for the heat input, making CMT have low heat input suitable for welding aluminium and thin sheets [43]. CMT can be utilized with SynchroPulse [69].

As already stated MIG welding is a traditional welding method, and is widely used today. There are some reasons why this is the case. Firstly, this process has a high melting rate and welding speed. Secondly, it is also possible to MIG weld in forced positions. Thirdly, the standard MIG setup has a small investment cost. Fourthly, the process has excellent appearance of welded joints and the process can easily be automated [32].

It should, however, be said that the method has some disadvantages too. Firstly, there is a risk of general welding errors. Secondly, slow welding errors may occur due to leakage of liquid metal in front of the electric arc. Thirdly, a relatively complicated welding training is needed for welding high alloy steels and non-ferrous alloys. Fourthly, it is difficult to arc weld aluminium due to the relatively low melting point compared to the oxide layer (Al_2O_3). This oxide layer is something that constantly form on the surface, and means that this layer must be removed before arc welding aluminium alloys [32].

2.3.2 Fusion Weld zones

During fusion welding two distinctive zones emerge. These are called the fusion zone (FZ) and the heat affected zone (HAZ). They both have unique microstructural features and properties, different from the microstructure far from the weld. The zone far from the weld is called the base material [9]. An illustration of the different weld zones is given in figure 9.

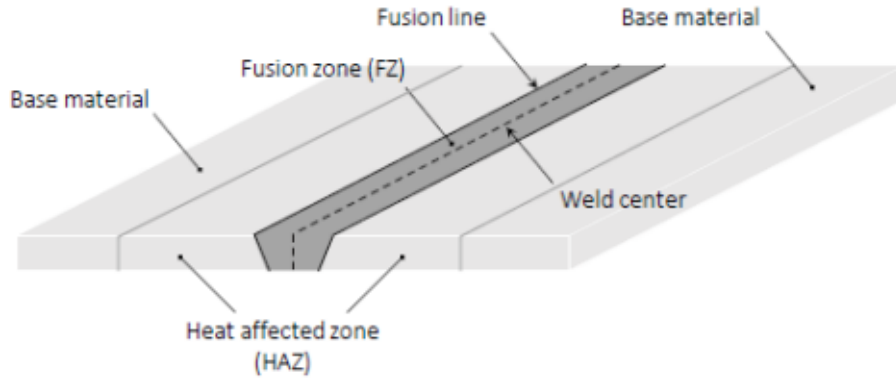


Figure 9: An illustration of the different zones in a fusion welded plate [26].

The properties of the FZ arises from the melting of parent material and the fact that this is where the maximum temperature is found during welding. The grains act as seed crystals for the initial solidifying material in the semisolid interface between the FZ and the HAZ, meaning that the coarseness of newly formed grains will be determined by the coarseness of the grains in the interface. The direction of the grain growth will be similar to the direction of the maximal thermal gradient, perpendicular towards the center of the weld. This gives all newly formed grains a columnar shape. Near the weld centre, the grain structure usually becomes equiaxed [25]. Equiaxed grains are able to nucleate either on detachments from the columnar zone, or from potential grain refining elements added to the filler material [13]. A general solidification structure in welds is presented in figure 10.

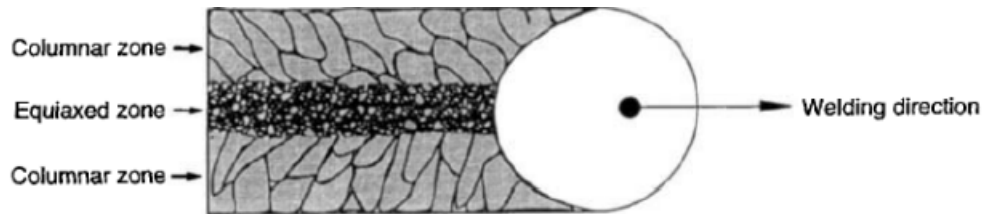


Figure 10: The solidification structure in fusion welds [25].

In the HAZ, the elevated temperatures lead to significant strength reductions. Even though the temperature in the HAZ does not reach melting temperature during welding, the temperature will cause dissolution or growth of β'' particles. The region of the HAZ close to the FZ is called the fully reverted region. Here the temperature can be approximately 500°C , a temperature high enough to solution heat treat the material and facilitate natural aging during room temperature storage [25].

As the distance from the weld centre decreases the temperature also decreases, preventing the precipitates from fully dissolving. With temperatures from about 250°C to 500°C , this part of the HAZ is called the reverted region. Large particles will coarsen, and small particles will dissolve, resulting in a decreased volume fraction of particles. As time progresses after welding, moderate reprecipitation occurs. Enhancement of reprecipitation can be done by employing heat. This process is called post weld heat treatment (PWHT). The heating will initiate artificial aging, but the weakest area of the partly reverted region will be depleted of solute Si and Mg, making reprecipitation of β'' particles by PWHT ineffective [53, 25]. Figure 11 shows the strength level of the various regions in the HAZ.

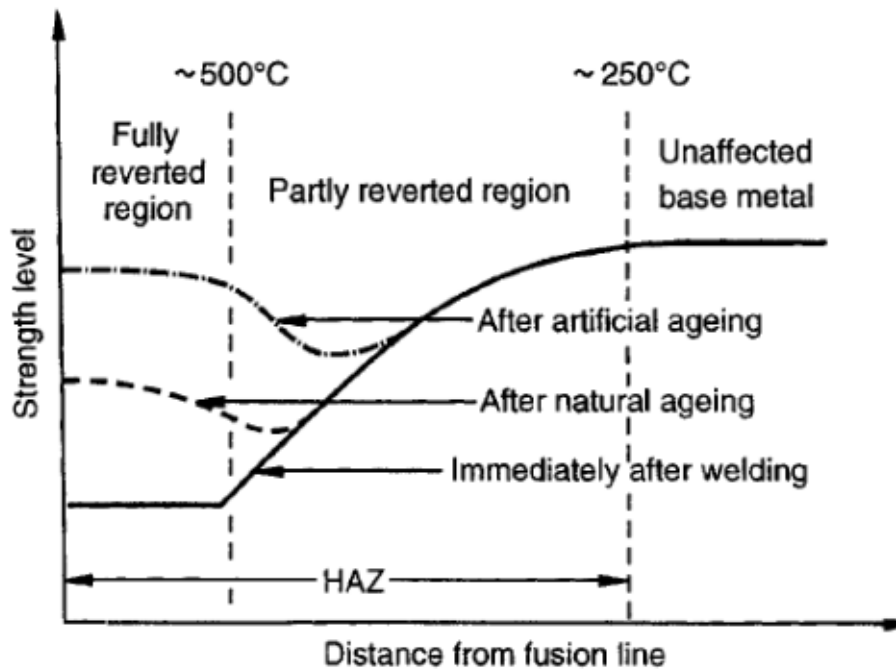


Figure 11: The strength in the HAZ, shown for three cases: immediately after fusion welding, after NA and after AA [25].

2.3.3 Friction Stir Welding

FSW is a relatively new solid-state joining process, invented at The Welding Institute of UK in 1991 [73]. The technique produces welds with a fine microstructure, and good mechanical properties. In 2005 FSW was considered to be the most significant development in metal joining for a decade [46].

The concept between the method is that a non-consumable rotating tool with a specially designed pin and shoulder is inserted between the plates that shall be joined. It then travels along this line, and produces a joint. This tool both heats the plates that shall be welded and it moves the material to produce the joint. The heat is produced through Coulomb friction between the the tool and the plates, and plastic deformation of the plates. Local heating softens the material around the pin, and combination of tool rotation and translation leads to movement of material from the front of the pin to the back of the pin. Because of different possible pin geometries, the material flow in FSW can be quite complex. The welded material undergoes intense plastic deformation at elevated temperatures, leading to fine and equiaxed grains [46].

FSW consumes less energy than conventional welding methods, due to its energy efficiency. In addition, the method does not involve any filler material, removing any issues involving changing the composition of the alloy, which is an issue in fusion welding. FSW can also be applied to different geometries, and not just plates as is the case for the main problem of this report. FSW works for butt joints, lap joints, T butt joints and fillet joints [46].

Still, to obtain a good weld using FSW is not guaranteed. Based on the energy input, three different types of defects can occur. Excess flash is characterized by that the working tool has penetrated further into the metal plate than it should have done, cavity defects can be seen as cavities (pores) in the stir zone and tunnel/wormhole can be seen as Groove-like defects are visible from the top of the weld [3].

How these different defects can form depending on the input parameters to the welding process, is summarized and given in figure 12.

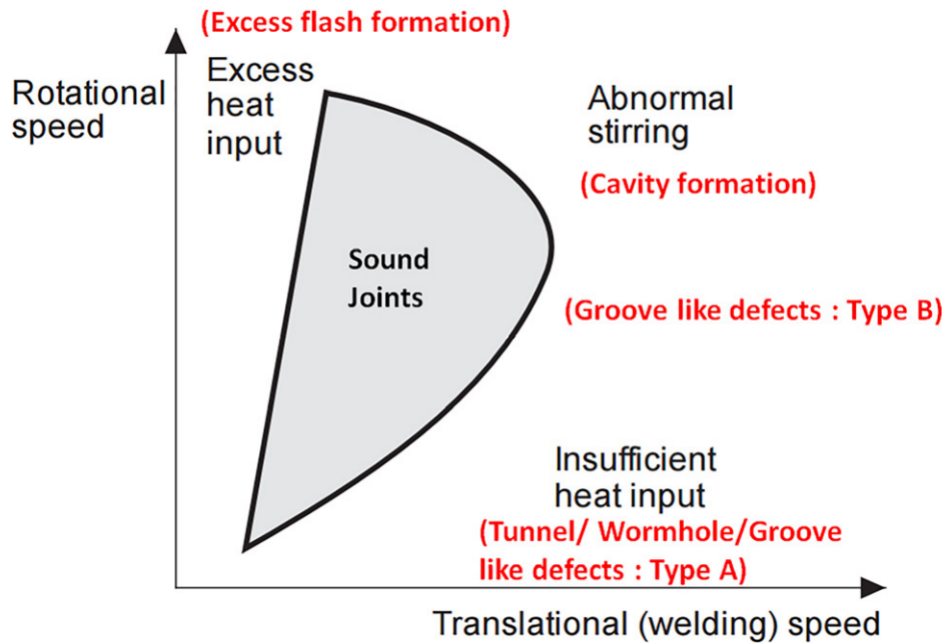


Figure 12: The relationship between process parameters and different defects. The region called Sound Joints is where the good welds are obtained. The figure is taken from [3].

It has been shown that an increase in tool plunge force can reduce the tunnel and cavity defects [3].

Wormhole and tunnel defects are formed if the ratio of welding speed to rotational speed is high. It has been shown that an increase in welding speed leads to more and bigger wormhole defects. In addition, too low tool plunge force can also lead to formation of these defects [3].

When the tool speed is too high, and the rotation speed is too low, groove-like defects will appear on the top of the weld. These defects are also caused by insufficient heat input. These defects have been shown to increase in size when the tool velocity is increased [3].

It has been shown that preheating of FSW has a number of benefits [81]. Not only will this reduce the hardness of the metal that is welded, meaning that the working tool experiences less friction, and can serve a longer lifetime, but it is also shown to have benefits when it comes to mechanical properties. Yaduwanshi *et al.* reached a maximum tensile strength of 93 % of the strength of the base material when preheating the material, while only 78% was reached using conventional FSW [81]. However, it should here be noted that this investigation used a 6061 aluminium alloy. Therefore similar results should not be expected for different compositions.

Something found by Yaduwanshi *et al.*, is that increasing the preheating before FSW, will increase the temperature of the process. However, it should be noted that these results were obtained by local preheating [81].

2.3.4 Friction Stir Weld Zones

The weld zones resulting from FSW are different than those arising after more traditional arc welding. Primary the fusion zone is replaced with a stir zone (SZ), as no melting occurs during FSW. There is also one more zone between the SZ and HAZ called the thermomechanically affected zone (TMAZ). In addition, the HAZ can be found further from the weld centre in FSW compared to arc welding. Figure 13 is a micrograph of a typical FSW profile, highlighting the different zones.

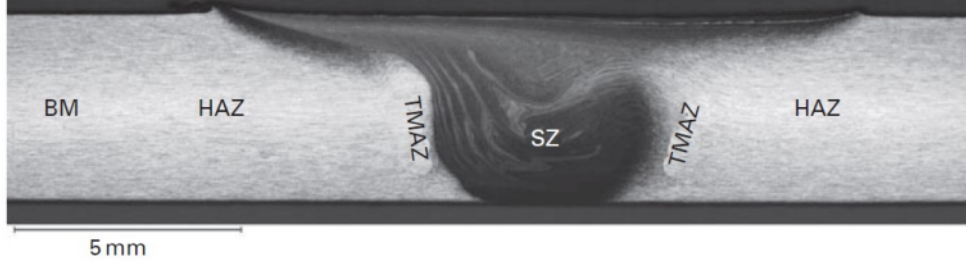


Figure 13: The profile of the cross section of a FSW alloy [36].

Considering the SZ, significant plastic deformation and temperatures over 500°C may result in solution heat treatment. This again, may recrystallize the metal, depending on the recrystallization resistance. Recrystallization will result in both a fine and equiaxed grain structure and a reduced dislocation density in the SZ. The diameter of the SZ tends to exceed the pin dimensions, but being smaller than the shoulder. Often the SZ extend from top to bottom of the weld [36].

The TMAZ can be found adjacent to the SZ. This zone will experience lower levels of plastic deformation and temperatures compared to the SZ. Still, closest to the SZ, grains may be rotated 90° , indicating substantial plastic deformation. Further from the weld centre the plastic deformation is less. The temperatures in the TMAZ range from 350 to 450°C , leading to ageing and annealing. Softening from the annealing will be compensated for by the work hardening effect of plastic deformation close to the SZ [36].

In the HAZ, there is no plastic deformation. Temperatures are between 250 and 350°C , and no changes in the grain structure will occur in this region. This means that the grain structure will be a similar to the one found in the base material. Still the elevated temperatures will cause recovery of cold work and coarsening of precipitates, reducing the strength [36].

2.4 The relation between Engineering Stress and Strain, and True Stress and Strain

When external tensile loading is applied on a metal, both elastic and plastic deformations will occur. Firstly, the elastic deformation will happen. This deformation has a linear relationship between load and extension. Plastic deformation will occur later, and be nonlinear. To calculate engineering stress, σ_E , and strain, ϵ_E , the two relations external load, P , and extension are used. This is described in equations 3 and 4 [17],

$$\sigma_E = \frac{P}{A_0}, \quad (3)$$

$$\epsilon_E = \frac{L_f - L_0}{L_0} = \frac{\Delta L}{L_0}. \quad (4)$$

The parameter A_0 is the original cross-sectional area of the specimen, L_0 is the original length of the specimen and L_f is the final length of the specimen [17].

An observation to be made from the equations above, is that engineering stress and strain uses the initial cross section of the specimen for calculating stress and strain. This is a simplification as the specimen will become thinner as the test progresses. So, true stress and strain will use the instantaneous cross section, A , instead [17].

To find a relation between engineering stress and strain, and true stress and strain, it is assumed no volume change in the specimen. When combining this assumption with the equations for engineering stress and strain, it is possible to obtain equation 5 [17],

$$A \cdot L = A_0 \cdot L_0 \Rightarrow \sigma_T = \frac{P}{A} = \frac{P}{A_0} \cdot \frac{L}{L_0} = \sigma_E (1 + \epsilon_E). \quad (5)$$

True strain is defined as the instantaneous increase in length. This gives the following calculations, resulting in equation 6 [17],

$$\epsilon_T = \int \frac{dL}{L} = \ln \left(\frac{L}{L_0} \right) = \ln \left(\frac{L_0}{L_0} \cdot \frac{\Delta L}{L_0} \right) = \ln (1 + \epsilon_E). \quad (6)$$

2.5 Simulation of the temperature development for medium thick plates

The reason why it is important to know how the temperature changes during welding, is because the metallurgical reactions are very temperature sensitive. To understand which reactions have happened, and in how large quantity, it is necessary to know the entire thermal history of the metal. Therefore, Myhr and Grong have developed a model called weld thermal cycle program (WTCP). This program is calculating the heat in a given position of the metal during welding [34].

Because of the simplicity of both the equations and the necessary processing, this program solves the heat problem using an analytical solution. This approximation has proved to work well for fusion welding [34].

An approximation done to obtain simple analytical solutions for Fourier's second law of heat conduction, is that the thermal properties of the metal are constant and independent of temperature. In addition, the thermal properties are thought to do not change for a changing composition either. These two approximations both limit the applications for this model. However, by choosing a average value can make this model work [34].

For solving how the temperature changes at a given point during welding, there are different models existing. The difference between these models is the thickness of the welded profile. This WTCP uses the medium thick plate case [34].

The medium thick plate case considers a point heat source moving at constant speed across a wide plate of finite thickness, d . This solution assumes that the plate surfaces are impermeable to heat. Imaginary mirror reflections of the heat source with respect to the plate surfaces are incorporated to maintain a net flux of heat equal to zero. This is illustrated in figure 14 [34].

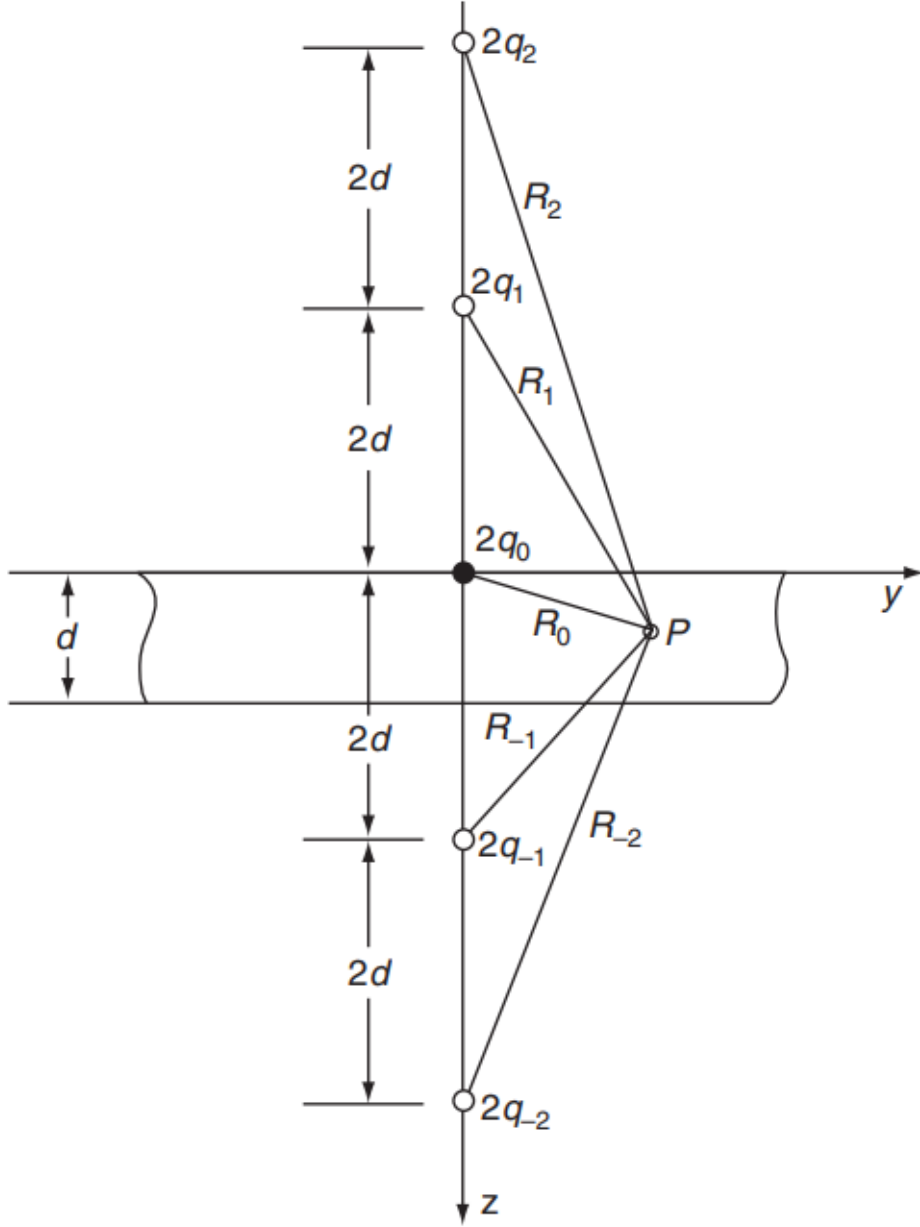


Figure 14: Illustration of the medium thick plate solution, showing real and imaginary point sources on a medium thick plate [34].

Figure 14 show that the reflections are located symmetrically at distances $\pm 2id$ perpendicularly to the real heat source, q_0 , that is located on the top of the plate. By including contributions from the mirror reflections, a solution of the three-dimensional differential equation for heat conduction may be obtained as a convergent series. This expression is given in equation 7 [34],

$$T - T_0 = \frac{q_0}{2\pi\lambda} \exp\left(-\frac{vx}{2a}\right) \sum_{i=-\infty}^{i=+\infty} \frac{1}{R_i} \exp\left(-\frac{vR_i}{2a}\right). \quad (7)$$

$T - T_0$ is the rise of temperature, q_0 is the power from the welding, v is the welding speed, λ , a is a material property and R_i is the distance shown in figure X. The distance R_i from a reference point P in the plate, can be described further by equation 8 [34],

$$R_i = \sqrt{x^2 + y^2 + (z - 2id)^2}. \quad (8)$$

When considering the cross-section of a weld, it is given that the temperature is highest close to the fusion zone. It will decrease quite fast as the distance decreases. From the paper made by Myhr and Grong, these isotherm lines were plotted for temperatures relevant for aluminium welding (given here as figure 15). It is possible to see that the isotherm lines have a circular shape close to the fusion zone, and later becomes more vertical further from the heat input. It is assumed that these isotherms will be completely vertical if the distance from the fusion zone is big enough [34].

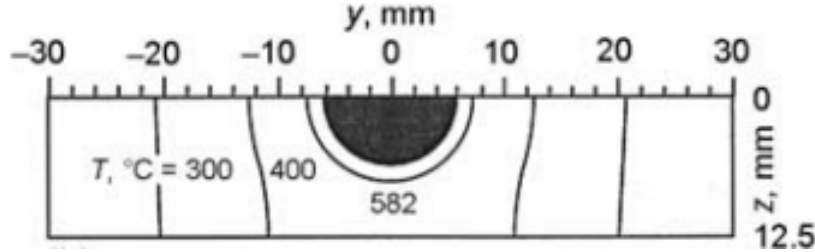


Figure 15: How the isotherm lines look for a cross section of an aluminium weld. The figure is taken from [34].

2.6 Simulation of precipitation, work hardening and strength for Al-Si-Mg alloys

As the nature of age hardening of Al-Si-Mg alloys depends on how the microstructure has become as a result of previous steps, it is not possible to model these cases analytically. Therefore the nanostructure model (NaMo) model is a finite difference numerical program. This has been developed over nearly two decades (2001-2018) [52, 53, 54, 55, 56], and is used to simulate precipitation, work hardening and strength for Al-Si-Mg alloys. The initial program (in 2001) was quite simple, and did only calculate the microstructure and material strength for Al-Si-Mg alloys when cooling from the solution heat treatment temperature. The later versions, on the other hand, is able to calculate the strength and hardness of aluminium alloys with different compositions, during different heat treatments and during deformation [52, 53, 54, 55, 56].

Since the NaMo model is calculating a lot of different material properties, the different parts of the model has been put into different submodels. An illustration of these models are shown in figure 16 [56]. This figure also shows how the different submodels are connected to each other.

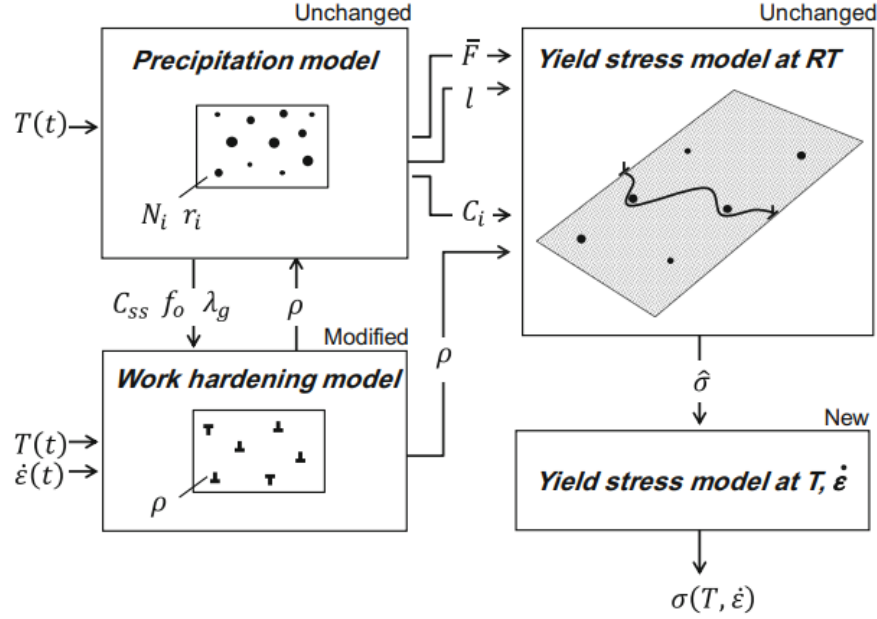


Figure 16: The different submodels in NaMo, showing what was unchanged, modified or new in 2018 [56].

An explanation of the different submodels is given below. Here the most essential assumptions and equations in NaMo is given.

2.6.1 Precipitation model

The short version of what the precipitation model does, is to calculate the microstructure in Al-Si-Mg alloys. Inputs for these calculations are the chemical composition and the thermal history.

The more complicated version, on the other hand, explains how the precipitation model is able to calculate the microstructure in Al-Si-Mg alloys for a number of different thermal processes. These include cooling from solution heat treatment, room temperature storage and natural aging, cold deformation, artificial aging, welding and post weld heat treatment. Theory used in the precipitation model for each of these thermal processes is presented below.

The first processing step the precipitation model must be able to describe, is cooling from the SHT temperature. As previously mentioned, quenching will result in a SSSS, while slower cooling will make precipitates dissolve. According to the model slow enough cooling rates will resolve in β' and even β particles, meaning that AA cannot give β'' precipitates [52].

After reaching room temperature, the model must be able to understand what happens to Al-Si-Mg alloys at room temperature storage and NA. When investigating this process, Murayama and Hono and Takaki *et al.* [48, 70] found that if the metal is kept between room temperature and 70°C between SHT and AA, clusters will form. These will survive a certain amount of time during the AA, and tie up solute that otherwise would have contributed to formation of β'' -particles. Higher storage temperatures, on the other hand, will lead to GP zone formation [48, 70].

What is clear is that in order to make a functioning NA model, evolution of clusters with time for different deformation conditions must be described. In addition, the mathematical description must be able to promote free exchange of the solute between the different precipitates [55].

The numerical code is based on the flexible Kampmann-Wagner formalism [55]. In practice, this means that two separate particle size distributions are used. One of these captures the cluster evolution during natural aging, while the other one describe β' and β'' formation during artificial

aging. This means that the model for natural aging and the model for artificial aging contain different nucleation and rate laws, in addition to different input parameters. Still, they are linked through the continuity equation that keeps a record of the amount of solute being tied-up as precipitates [50, 78, 28].

Following room temperature storage, Al-Si-Mg alloys tend to go through AA. The most essential assumption done in the NaMo model for this step, is that an uniform distribution of β'' particles will form in the matrix [53].

Typically, welding happens after AA. During this process, high temperatures will make the small β'' particles unstable and they will begin to dissolve. At the highest temperatures the model understands that some of the β'' will be able to return as the temperature drops after the welding is done. Further from the fusion line, on the other hand, coarse rod shaped β' particles will form instead. These particles will grow rapidly as there is a lot of extra solute coming from the previously dissolved β'' particles. As the β' particles are much larger in size than the β'' particles, the precipitate density will decrease in these regions [55].

During cold deformation, the generated dislocations will affect the nucleation process in different ways. One of these, is that they provide favorable sites for heterogeneous nucleation of β' precipitates during AA. At the same time, dislocations act as sinks for excess vacancies and solute atoms. This means that precipitate-free zone (PFZ) will form around the dislocations and the matrix nucleation rate decreases locally due to depletion [54].

When dislocations are present, there is a competition between nucleation of β'' and β' . It is known that matrix nucleation of β'' dominates for low dislocation densities, while nucleation of β' happens the most for high dislocation densities. In between, both of these precipitates may form [54].

The last processing step that the model is able to describe is PWHT. This treatment is done to increase the material strength after welding, and will result in a re-precipitation of β'' where the temperature in HAZ has been high. According to classical nucleation theory, the amount of re-precipitation depends on the concentration of both the matrix vacancy and the Mg and Si in solid solution. From this, it follows that re-precipitation should happen most where the matrix is the most "erased" after welding. This happens close to the fusion line, as this region has both a high solid solution concentration and a high amount of quenched in particles. In regions where the temperatures were lower, it is less β'' formation. This is because there is less vacancies and solid solution. This gives a permanent soft region in the HAZ, also after PWHT [53].

The first step of making a functioning mathematical model of this theory is a proper definition of the different particles. In NaMo both the metastable β'' and β' particles, and the stable β particle are given as small equilibrium particles with uniform thermodynamical properties and a given composition. As a simplification, the thermal stability is given through the Gibbs-Thomson equation. By previous verification of the model, this approximation seems to capture the metastable solvus boundary of Al-Si-Mg alloys [55].

An advantage with using the Gibbs-Thomson equation, is that more complicated cases can be simulated. This is because complicated industrial alloys can be seen as binary alloys, where all the particles is a part of the same particle distribution. Since the memory of this particle size distribution is included in the calculations, the memory of previous processing steps are included in the thermal history [55].

The precipitation model is made as a finite difference formulation of the classical precipitate model made by Kampmann and co-workers [52, 28] and Langer and Schwartz [33]. The particle distribution is divided into a series of discrete size classes, each represented by a control volume. A standard discretisation of the governing evolution equation, makes it possible to calculate the flux of particles in and out of the control volume at each time step during thermal cycling [50].

The precipitation model can be divided in three parts. These are a nucleation law (predicts the number of stable nuclei that form at each time-step), a rate law (calculates either the dissolution or the growth rate of each discrete particle size class) and a continuity equation (keeps record of the amount of solute being tied up as precipitates) [54]. The rest of this subsection will describe these laws.

As a basis for the nucleation law, classical nucleation theory states that nuclei are formed due to localized compositional fluctuations. These happen statistically in the matrix of the solid solution. If both the incubation period is neglected and the possible effects from elastic coherency strains around the particles are ignored, the nucleation rate, j , can be described through equation 9 [2],

$$j = j_0 \exp\left(-\frac{Q_d}{RT}\right) \exp\left(-\frac{\Delta G^*}{RT}\right). \quad (9)$$

The only problem with the equation given above, is that the effect of quenched in vacancies are neglected. This term is important for PWHF. Since classical nucleation theory is incomplete in this field, vacancies-solute interactions are difficult to model [53]. Qualitatively, it is assumed that the term j_0 (pre-exponential factor) can be scaled with the equilibrium vacancy concentration at the peak temperature, T_p , during the process. The nucleation law used to describe this is given as equation 10 [55],

$$j = j_0 \exp\left(-\frac{Q_d}{RT}\right) \exp\left(-\frac{\Delta G^*}{RT}\right) \exp\left(-\frac{\Delta H_v}{R} \left(\frac{1}{T_p} - \frac{1}{T_{ss}}\right)\right). \quad (10)$$

The form of equation 10, makes it simple to implement in the model. An assumption that can be drawn from the equation, is that the total number of nucleation sites is proportional with the equilibrium concentration of vacancies in the HAZ at the peak temperature, T_p [55]. This means that diffusion and annihilation of vacancies near grain boundaries during subsequent cooling/reheating is neglected, but it is assumed that this still will work as a valid approximation. A property with equation 10, is that it will be reduced to equation 9 when quenching from the solution temperature, T_{ss} . This means that no recalibration of the parameters is necessary to use this formula [55].

Since NaMo is able to differentiate between AA and NA, and the separate particle distributions of β' and β'' , some of the parameters of equation 9 and 10 changes depending on the case of the nucleation. This is relevant for the pre-exponential factor, j_0 , and the energy barrier for heterogeneous nucleation, ΔG^* . The values for these parameters are given in table 1. The other parameters, on the other hand, remains constant for all cases. Q_d is the activation energy for bulk diffusion of magnesium in aluminum or diffusion of magnesium across the cluster/matrix interface (J/mol), R is the universal gas constant (8.314J/Kmol) and T is the temperature (K) [55].

Table 1: Expressions for the different nucleation laws implemented in the NaMo model [55].

Model	Expression for j_0	Expression for ΔG^*
NA-model (cluster formation)	$j_0^{c1}(1 - \rho/\rho_c) + j_0^{c2}$	$\frac{(A_0^c)^3}{(RT \ln(\bar{C}/C_e^{Mg}) - \Delta G_s)^2}$
AA-model (nucleation of β'' in Al matrix)	$j_0^m(1 - \rho/\rho_c)$	$\frac{(A_0^m)^3}{(RT \ln(\bar{C}/C_e^{Mg}))^2}$
AA-model (nucleation of β' at dislocations)	j_0^d	$\frac{(A_0^d)^3}{(RT \ln(\bar{C}/C_e^{Mg}))^2}$

The different parameters given in this table, are defined as following: j_0^{c1} , j_0^{c2} , j_0^m and j_0^d are pre-exponential factors, ρ is the matrix dislocation density, ρ_c is the critical dislocation density, A_0^c , A_0^m and A_0^d are parameters related to the energy barrier for heterogeneous nucleation, ΔG_s is the misfit strain energy, C_e^{Mg} is the equilibrium concentration of magnesium at cluster/matrix or particle/matrix interface and \bar{C} is the mean solute concentration in matrix [55].

When it comes to the ΔG_s term, that is included in the NA-model given in table 1, Myhr, Grong and Schäfer found that Al-Si-Mg alloys has values between 1.1 and 7.7 [64]. They chose to implement a value of 2.7 kJ/mol as a default value in the model [55].

When it comes to how the model describes AA, the two equations given in table 1, makes it clear that the the matrix nucleation of β'' dominates at low dislocation densities, while nucleation of β' at dislocations is the overriding mechanism when $\rho_g \leq \rho$. In between, both types of precipitates may form at the same time [55].

A last note about the precipitation equations, is that they neglect the diffusion and annihilation of vacancies at grain boundaries and incoherent particle/matrix interfaces during subsequent cooling/reheating. Still this is considered a reasonable approximation [53].

When it comes to the growth laws, expressions for what is used in the NaMo model, are summarized in table 2.

Table 2: Expressions for the different growth laws implemented in the NaMo model [55].

Model	Expression for the Growth Rate
NA-model (cluster formation)	$\frac{dr}{dt} = M_0 \exp\left(-\frac{Q_d}{RT}\right) (\bar{C} - C_i^{Mg})$
AA-model (nucleation of β in Al matrix, and in Al matrix and nucleation of β' at dislocations)	$\frac{dr}{dt} = \left(\frac{\bar{C} - C_i^{Mg}}{C_p^{Mg} - C_i^{Mg}}\right) \left(\frac{D_{eff}^{Mg}}{r}\right)$, where $D_{eff} = D^{Mg} \left[1 + \left(\rho a_c \frac{D_c^{Mg}}{D^{Mg}}\right)\right]$

In the NA model, interface controlled growth is assumed. The cluster evolution at room temperature is calculated from the standard expression relating dr/dt to the mean solute concentration \bar{C} and the interface concentration of magnesium, C_i^{Mg} [4]. The value of C_i^{Mg} is updated for each time step through the extended thermodynamic model and Gibbs-Thomson equation, something that makes the rate laws describe the subsequent reversion of the clusters during AA. This corresponds to the situation where $C_i^{Mg} > \bar{C}$, and dr/dt becomes negative. At the same time, the temperature dependence of the reaction rate is captured by an Arrhenius type of relationship, employing published data for the pre-exponential mobility term, M_0 , and the activation energy, Q_0 , for magnesium diffusion across the cluster/matrix interface [4]. These values are used as default values in the model [55].

In the extended AA model, diffusion controlled growth is assumed and implemented [50, 51]. The diffusion coefficient of magnesium allows for pipe diffusion through the dislocation core following cold deformation. The relationship between the effective diffusion coefficient, D_{eff}^{Mg} , the bulk diffusion coefficient, D^{Mg} , the core diffusion coefficient, D_c^{Mg} , the matrix dislocation density, ρ , and the cross-sectional area of pipes, a_c is identical to what is frequently quoted in scientific literature [62, 61]. This means that all necessary input data can be obtained from well-established sources and used as default values in the numerical code [61]. The parameter C_p^{Mg} is the concentration of magnesium inside clusters or particles.

In addition, an expression for how large the particles will become is implemented through derivation from the Gibbs-Thomson equation. Equation 11 gives an explicit expression for the critical radius r' , where the particle will neither grow or dissolve [1],

$$r' = \frac{2\gamma V_m}{RT} \left(\ln \left(\frac{\bar{C}}{C_e} \right) \right)^{-1}. \quad (11)$$

γ is the particle/matrix interfacial energy, V_m is the molar volume of the precipitates and C_e is the equilibrium concentration at cluster/matrix or particle/matrix interface [52].

Based on equation 11, it is clear that r' depends on C_e . This means that the thermal stability of the precipitates is sensitive to changes in temperature, something that happens during heat treatment. It can be seen that heating leads to particle dissolution, while cooling or isotherm annealing leads to nucleation, growth and coarsening. From this it is clear that the thermal program has a huge effect on the microstructure. It is clear that to get a correct result, the microstructure must follow a numerical scheme to take account for the "memory" of the microstructure [52].

The mean solute content in the matrix, \bar{C} , is calculated from the continuity equation to obtain the instantaneous values of the nucleation and growth rates in the precipitation model. This equation assumes that all precipitates have identical chemical composition and mass density [50, 51, 52, 54, 53]. These assumptions largely simplify the mass balance without contributing to loss of predictive

power [51, 52, 53, 54]. Since the model is calculating what happens for two separate particle size distributions, two separate number of particles, N_i and N_j , and discrete radius intervals, r_i and r_j , must be included in the equation. This equation is given as equation 12,

$$\bar{C} = C_0^{Mg} - (C_p^{Mg} - \bar{C}) \left(\sum_i \frac{4}{3} \pi r_i^3 N_i + \sum_j \frac{4}{3} \pi r_j^3 N_j \right). \quad (12)$$

In equation 12, the volume fraction of clusters and hardening precipitates are calculated through separate summation formulas. However, since all particles are assumed to have the same magnesium content, their volume fraction, f , can also be calculated from the composition parameters C_0^{Mg} , \bar{C} and C_p^{Mg} . This relation is given as equation 13 [55],

$$f = \frac{C_0^{Mg} - \bar{C}}{C_p^{Mg} - \bar{C}}. \quad (13)$$

This equation shows that the continuity equation actually is a "lever rule" that takes the inherent constraints provided by the phase diagrams into account [55].

The thermodynamic model providing input data for C_e^{Mg} and C_i^{Mg} is a simplified quasi-binary description of the phase relations within the Al-rich corner of the Al-Mg-Si phase diagram (see figure 5) [51, 53]. Corresponding data for the metastable phases also exist [63], and the same approach can be employed to find the thermodynamic solvus temperatures for the clusters that form during NA as a function of magnesium content. When using reported values for the stable α -Al- β system as a starting point for the curve fitting, a general equation for C_e^{Mg} is obtained [53]. This relation is given as equation 14,

$$C_e^{Mg}(\text{wt pct}) = C_s \exp\left(-\frac{Q_s}{RT}\right) = 290 \exp\left(-\frac{(41000 - \Omega_c)}{RT}\right). \quad (14)$$

Ω_c is a correction term which accounts for the reduced thermodynamic stability of the clusters compared with the other metastable phases β , β' and β'' . Q_s is the solvus boundary enthalpy [55].

From equation 14 it follows that the hardening β' and β'' precipitates are characterized by the same solvus boundary enthalpy, Q_s , as the equilibrium phase, β . Therefore it is assumed that the reduced stability of the metastable phases are due to the smaller particle sizes compared to β [8, 52, 53]. The clusters, on the other hand, have a highly different atomic structure, and have their own equilibrium solvus within the phase diagram. This is allowed for through the Ω_c parameter in the expression for Q_s [55].

The value of Ω_c has been determined by calibrating equation 14 to reported data for cluster formation in Al-Mg-Si alloys [63]. A default value of 18.3 kJ/mol is used in the model [55].

It is possible to calculate the magnesium concentration at the cluster/matrix interface, C_i^{Mg} , through the Gibbs-Thomson relation [50, 51, 52, 53, 54]. This is given in equation 15 [55],

$$C_i^{Mg} = C_e^{Mg} \exp\left(\frac{2\gamma_c V_m}{rRT}\right). \quad (15)$$

V_m is the molar volume of the clusters, and is assumed to be constant and the default value used in the model is $7.62 \times 10^{-5} \text{m}^3/\text{mol}$ [51, 52, 53, 54]. Since V_m is fixed, the cluster/matrix interfacial energy, γ_c , is adjusted so that equation 15 gives realistic values for C_i^{Mg} [63]. The default value in the model is 0.02 J/m² [55].

2.6.2 Strength model

It is assumed that the particles are spherical and of equal size. This makes it possible to derive equations based on classical analytical solutions for the dislocation-particle interaction [52].

Based on a equation described by Deschamps and Brechet [12], Myhr, *et al.* expressed an equation for the increase in overall macroscopic yield strength, σ_p , due to the mean obstacle strength, \bar{F} [12, 19, 47]. This expression is given as equation 16 [52],

$$\sigma_p = \frac{M}{\mathbf{b}\bar{r}}(2\beta Gb^2)^{-1/2} \left(\frac{3f}{2\pi}\right)^{1/2} \bar{F}^{3/2}. \quad (16)$$

M is the Taylor factor, \mathbf{b} the magnitude of the burgers vector, \bar{r} is the mean particle size, f is the volume fraction, β is a constant close to 0.5 and G is the shear modulus of the aluminium matrix [52].

The mean obstacle strength is combination of weak (shearable) and strong (non-shearable) particles, and can be estimated numerically through equation 17 [52],

$$\bar{F} = \frac{\sum_i N_i F_i}{\sum_i N_i}. \quad (17)$$

F_i is the obstacle strength corresponding to the correct number density of particles, N_i , and size class, r [52].

The parameter F_i does however depend on the the particle radius r_i . For weak particles, it can be assumed that F_i is proportional to the particle radius r , given that this radius is below the critical radius for shearing, r_c [12, 22]. This can be expressed as equation 18 [52],

$$\bar{F}_i = 2\beta G\mathbf{b}^2 \left(\frac{r_i}{r_c}\right), \text{ for } r_i \leq r_c. \quad (18)$$

For strong particles ($r_i > r_c$), the obstacle strength, F_i , is constant and independent of particle size [12, 22],

$$\bar{F}_i = 2\beta G\mathbf{b}^2. \quad (19)$$

2.6.3 Overall hardness and yield strength

It can be assumed that the several strengthening mechanisms that operate at room temperature can be added linearly. This is described in equation 20 [52],

$$\sigma_y = \sigma_i + \sigma_{ss} + \sigma_p. \quad (20)$$

σ_y is the macroscopic yield strength, σ_i is the intrinsic yield strength of pure aluminium, σ_{ss} is the yield strength from alloying elements in solid solution and σ_p is the yield strength from all precipitates. [52] This again can be converted to Vicker's hardness (HV) [25]. This follows equation 21 [52],

$$HV = 0.33\sigma_y + 16.0. \quad (21)$$

2.6.4 Work hardening model

To express the yield stress, the contribution from dislocations, σ_d , has to be found. The total dislocation density, ρ , is assumed to be the sum of all statistically stored dislocations, ρ_s , and the geometrically necessary dislocations, ρ_g . Their contribution to the yield stress, σ_d , is given in equation 22 [29],

$$\sigma_d = \alpha M \mu \mathbf{b} \sqrt{\rho_s + \rho_g}. \quad (22)$$

α is a constant with numerical value close to 0.3 and μ is the shear modulus for which the temperature dependence is accounted for through the equation 23 [67],

$$\mu = \mu_0 \left(1 - \frac{T}{T_m} \exp \left(\theta_g \left(1 - \frac{T_m}{T} \right) \right) \right). \quad (23)$$

μ_0 is the shear modulus at 0 K, T_m is the melting temperature of the material and θ_g is a material constant equal to 2.295 [56].

Something that should be noted, is that ρ_s and ρ_g affect the flow stress directly through equation 22 in addition to affect the precipitation structure that forms since nucleation of metastable β' particles along dislocation lines takes place to an increasing extent during aging when the dislocation density increases [71, 72]. In the NaMo model, this transition from matrix nucleation of β'' particles to nucleation of β' particles at dislocations with increasing ρ_s through back coupling from the work hardening model [56].

The Kocks-Mecking relationship gives the evolution of the statistically stored dislocations [30, 45]. This is given as equation 24 [56],

$$\frac{d\rho_s}{d\epsilon_p} = k_1 \sqrt{\rho_s} - k_2 \rho_s. \quad (24)$$

Dynamic recovery depends on temperature and strain rate, and k_2 can be correlated with the Zener-Hollomon parameter, according to Bergström and Hallén [7]. What is assumed, is that dislocation climb is the dominant dynamic recovery mechanism, and that diffusion of vacancies to dislocation cell walls is the rate controlling reaction, determining the climb rate [56].

The equations used in the NaMo model, is valid for plastic straining at room temperature, where the Zener-Hollomon parameter is high ($Z \gg Z_s$). The model also introduces a reference alloy state for a temperature of 0 K in the equations, and assumes that the reference alloy has a Taylor factor, M_r , that is equal to the Taylor factor of the actual material, M . From all of this, a final equation for the model is determined, and given here as equation 25 [56],

$$k_2 = k_2^0 \left(\frac{\mu}{\mu_0} \right) \left(\frac{C'_{ss}}{C_{ss}} \right)^{\frac{3}{4}} \left[1 + \left(\frac{Z_s}{Z} \right)^m \right]. \quad (25)$$

k_2^0 is the k_2 value for the reference alloy at 0 K, μ is the shear modulus for the actual alloy, while μ_0 is the shear modulus for the reference alloy. C'_{ss} is the effective solid solution concentration for the reference alloy (set to 1wt% in the model), and C_{ss} is the effective solid solution concentration for the actual alloy. Z_s and m are constants [56].

As for statistically stored dislocations, the evolution law for geometrically necessary dislocations can be expressed by two terms. One of these is for storing the dislocation, while the other is for dynamic recovery. The evolution law for ρ_g used in the NaMo model is given in equation 26 [54],

$$\frac{d\rho_g}{d\epsilon_p} = \frac{k_{1g}}{\lambda_g} - k_{2g} \rho_g. \quad (26)$$

k_{1g} is a characteristic material constant and ϵ_p is the plastic tensile strain. k_{2g} determines the rate of which dynamic recovery during plastic deformation depends on the actual solute content of the alloy, and the effect of strain rate and temperature can be included in this term. This makes the constant k_{2g} defined through equation 27 [30, 45, 75, 18, 54].

$$k_{2g} = k_{2g}^0 \left(\frac{f_0}{f'_0} \right) \left[1 + \left(\frac{Z_g}{Z} \right)^m \right]. \quad (27)$$

k_{2g}^0 is the dynamic recovery constant for the reference alloy where $Z \gg Z_g$ and $f_0 = f'_0$. It is assumed that k_{2g} is proportional to the volume fraction of non-shearable particles, f_0 [56].

When the precipitate structure remains constant during plastic deformation, at the same time as plastic straining is carried out through constant strain rate and temperature, the net contribution from dislocations hardening, σ_d , can be calculated by an analytical equation. This equation is derived by integrating the dislocation densities ρ_s and ρ_g from the equation 24 and 26, and substituting the values into equation 22. The expression is given in equation 28 [56],

$$\sigma_d = \alpha M \mu b \sqrt{\left(\frac{k_1}{k_2} \right) \left(1 - \exp\left(-\frac{k_2 \epsilon_p}{2} \right) \right)^2 + \left(\frac{k_{1g}}{\lambda_g k_{2g}} \right) (1 - \exp(-k_{2g} \epsilon_p))}. \quad (28)$$

In equation 28 effects of temperature and strain rate are included in the dynamic recovery constants k_2 and k_{2g} . Both of these depend on temperature and strain rate through the Zener-Hollomon parameter, Z [56].

A note that should be made, is that equation 28 cannot be used for a general situation including a non-constant strain rate or temperature. For those situations, σ_d has to be calculated numerically with a stepwise increase in time, where relevant solute and precipitate parameters (C_{ss} , f_0 and λ_g) are transferred to the work hardening model for each time step [55].

During AA, the dislocation density that came as a result of cold deformation, ρ , will be reduced due to static recovery processes occurring at elevated temperatures [57]. The static recovery model of Nes *et al.* [57, 68, 58] has been implemented in the model. This equation, describing $d\rho/dt$ is adopted to capture the dislocation annihilation, and is given as equation 29 [55].

$$d\rho/dt = -k_3 \rho^{3/2} \exp\left(-\frac{U_s}{RT} \right) \sinh\left(\frac{k_4 \sqrt{\rho}}{RT} \right). \quad (29)$$

U_s is the average activation energy for the solute diffusion constricting the dislocation movement, as defined in [68, 58]. k_3 and k_4 are two fitting parameters, which are separately calibrated by comparing the static recovery model to experimental data. The default values in the model are $k_3 = 5.68$ m/s and $k_4 = 0.0048$ Jm/mol after reported data by Furu *et al.* [21].

2.6.5 Solid solution hardening

The alloying elements Mg, Si and Cu each give a considerable solid solution strengthening, σ_{ss} , for aluminium alloys. These contributions are assumed to be additive giving equation 30 [60, 20],

$$\sigma_{ss} = \sum_j k_j C_j^{2/3}. \quad (30)$$

C_j is the concentration of a specific alloying element in solid solution, and k_j is the corresponding scaling factor [52].

A note about this formula is that for the elements Mg and Si, the concentrations C_{Mg} and C_{Si} will vary during heat treatment depending on the volume fraction of clusters and metastable particles.

When there is a high volume fraction of clusters and metastable particles, the consecration of both Mg and Si will be low, since the elements are removed from the matrix. This relation between elements dissolved in the matrix and elements as part of particles or clusters is integrated in the continuity equation described in the precipitation model.

2.6.6 Yield stress model

To include the effects of temperature and strain rate on the yield strength, a model based on obstacle limited dislocation glide has been chosen. The model is derived, based on the Orowan equation model that describes the relationship between the average speed of the mobile dislocations and the strain rate, and introduces the Gibbs free energy of cutting bypassing of barriers as a function of the applied stress [20, 31]. The resulting flow stress, σ , is expressed in equation 31 [20, 31],

$$\sigma = \hat{\sigma} \frac{\mu(T)}{\mu_0} \left\{ 1 - \left[\frac{RT}{\Delta G} \ln \left(\frac{\dot{\epsilon}_0}{\dot{\epsilon}_p} \right) \right]^{1/q} \right\}^{1/p}. \quad (31)$$

$\hat{\sigma}$ can be considered the yield stress at 0 K, meaning that the barriers are overcome in the absence of any thermal activation. ΔG is the total free energy corresponding to the activation energy required to overcome the obstacle without external stress. The constants p and q depend on the spatial distribution and shape of the obstacles [20, 31]. Their values can vary ($0 \leq p \leq 1$ and $1 \leq q \leq 2$) [20], but the influence of these changes are relatively small compared to sufficient large ΔG -values [20]. In the NaMo model, both of the constants are assumed to be 1, as this has been used as a reasonable approximation for the relevant alloys before [76].

A similar argument is made for the reference strain rate, $\dot{\epsilon}_0$. Since ΔG is sufficiently large, a constant strain rate of 10^6s^{-1} [20] is implemented in the NaMo model.

The previously developed room-temperature yield stress model can be coupled to the new model that includes the effect of temperature and strain rate. If the room temperature ($T_r = 298 \text{ K}$) and representative strain rate ($\dot{\epsilon}_r = 10^{-4} \text{s}^{-1}$) that was used when calibrating the room temperature yield stress model into equation 31 is used, the resulting flow stress, σ_y , can be expressed as equation 32.

$$\sigma_y = \hat{\sigma} \frac{\mu(T_r)}{\mu_0} \left\{ 1 - \left[\frac{RT_r}{\Delta G} \ln \left(\frac{\dot{\epsilon}_0}{\dot{\epsilon}_r} \right) \right]^{1/q} \right\}^{1/p}. \quad (32)$$

If a constant c_1 is used, equation 32 can be rewritten simply as $\sigma_y = c_1 \hat{\sigma}$, where the constant c_1 is given in equation 33,

$$c_1 = \frac{\mu(T_r)}{\mu_0} \left\{ 1 - \left[\frac{RT_r}{\Delta G} \ln \left(\frac{\dot{\epsilon}_0}{\dot{\epsilon}_r} \right) \right]^{1/q} \right\}^{1/p}. \quad (33)$$

After calibration of ΔG , equation 33 gives the output $c_1 = 0.83$. It is clear that the representative strain rate is approximated, giving an inexact solution. Still, since $\dot{\epsilon}_r$ is entering a logarithmic term in equation 33, this approximation is not critical for getting an exact value for c_1 [56].

After getting values for c_1 , it is easy to convert the yield stress at room temperature, σ_y , to a corresponding yield stress at 0 K, $\hat{\sigma}$. This value can be substituted into equation 31, to get a temperature and strain rate depending flow stress, σ [56].

3 Experimental

3.1 Chemical Composition

The chemical composition of the Al-Si-Mg alloy investigated in this thesis is given in table 3. This alloy follows a common industrial standard. This composition is a AA-6082.5 alloy.

Table 3: The chemical composition of the Al-Si-Mg alloy investigated in this thesis. All the values are given in wt%.

Si	Fe	Cu	Mn	Mg	Cr	Al
0.9	0.32	0.1	0.55	0.65	<0.001	Bal.

3.2 Plate preparation, Heating and Cooling

As described in section 1, the motivation for this master thesis, is to see if welding of large constructions can be done in a cheaper and simpler way than what is normal today. Therefore, this alternative processing has been tested and compared to a reference that is processed in a traditional way. The reference Al-Si-Mg alloy was in a T6 state.

General production of Al-Si-Mg alloys tend to result in large profiles, unsuited for experimental investigation. This meant that in order to start the heat treatment, the profiles first had to be cut into smaller pieces. This cutting was done using a bandsaw, and the plate dimensions were 75x150x6mm.

Before heating, holes were drilled so that the temperature in the plates could be measured. These holes had a thickness of 2mm in diameter, and was about 20mm deep. Only six holes were made, one hole for each of the different cooling experiment (cooling in warm water, air and oven at two different temperatures). The plate dimensions as well as the positioning of the holes can be seen in figure 17.

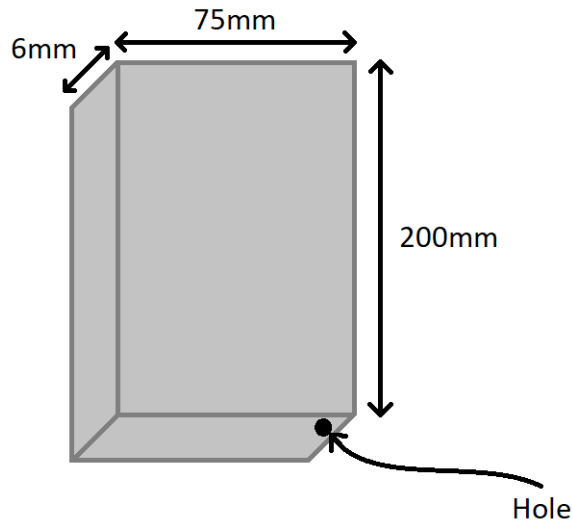


Figure 17: The dimensions of each plate, as well as the position of the hole

The plates were placed in a Nabertherm N17/HR Muffle furnace. Here the heating was done two separate times, one until 430°C and one until 550°C. The plates were in the oven for 30 minutes

before they were removed. The reference alloy came from an industrial produced T6 state, and was not heated in the oven.

When the plates were taken from the oven, the temperature measurements were turned on. As can be seen in figure 17, the temperature was measured inside the plates, and the temperature was logged ten times per second. The results from these two logins can be seen in figure 18 and 19.

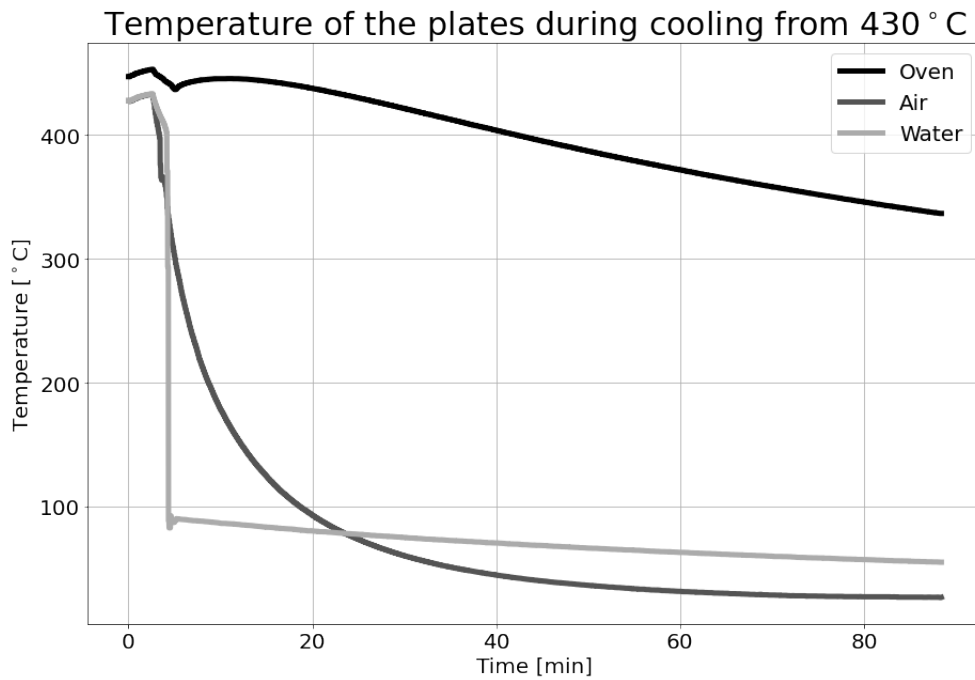


Figure 18: The temperature in the plates during cooling from 430°C

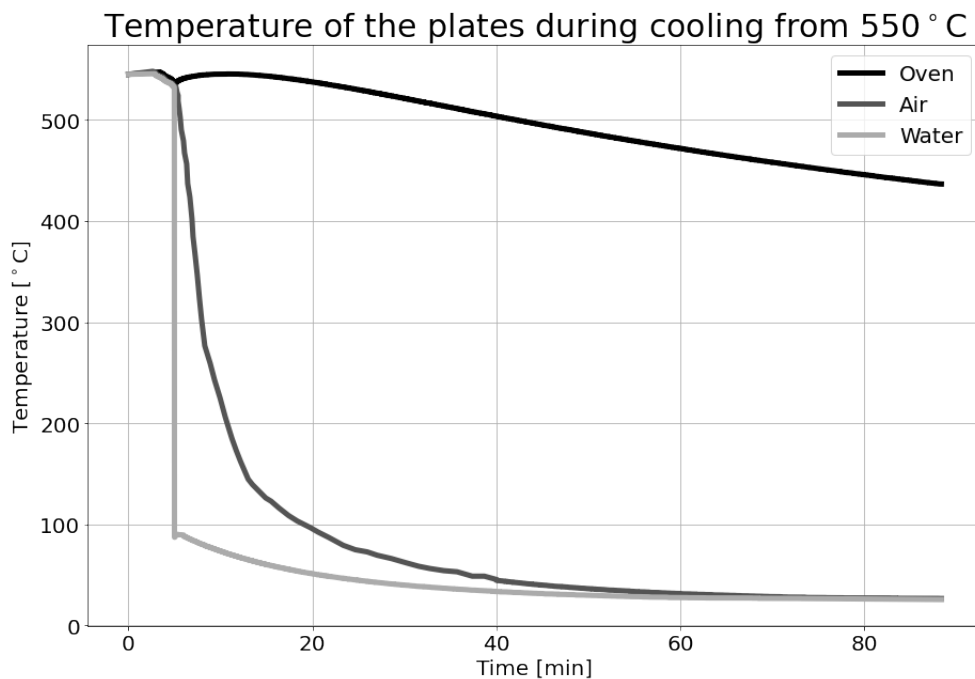


Figure 19: The temperature in the plates during cooling from 550°C

Later one side of the plates were milled down into a smooth surface suitable for welding. It was

these smooth surfaces that were welded together. For the plates that were FSW, the side had a I-shaped surface, while the plates that were MIG welded had a X-shaped surface. The X-shaped surface had an angle of 60° . This shape is illustrated in figure 20. Since an I-shaped surface is pretty self explainable, no illustration of this shape is given.

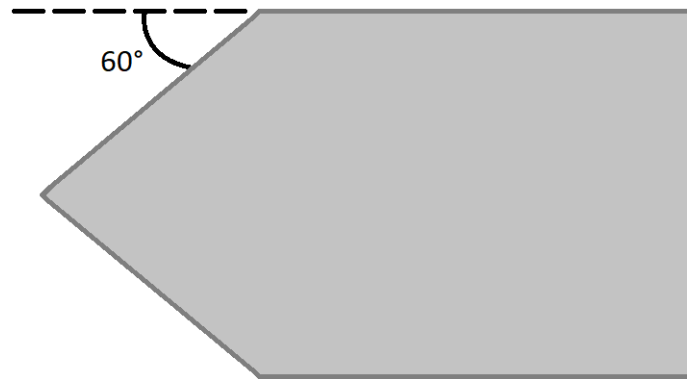


Figure 20: The X-shaped surface on the plates prepared for MIG welding. As can be seen in the figure, the angle was 60° .

3.3 Friction Stir Welding

The welding was done at SINTEF Manufacturing. Seven welds were done in total, two parallels for each of the heated cases, and one for the reference.

Three thermocouples were inserted in each plate, at the distances 5, 9 and 13mm from the weld centre. This is illustrated in figure 21. These temperature measurements were later used as inputs for the program NaMo.

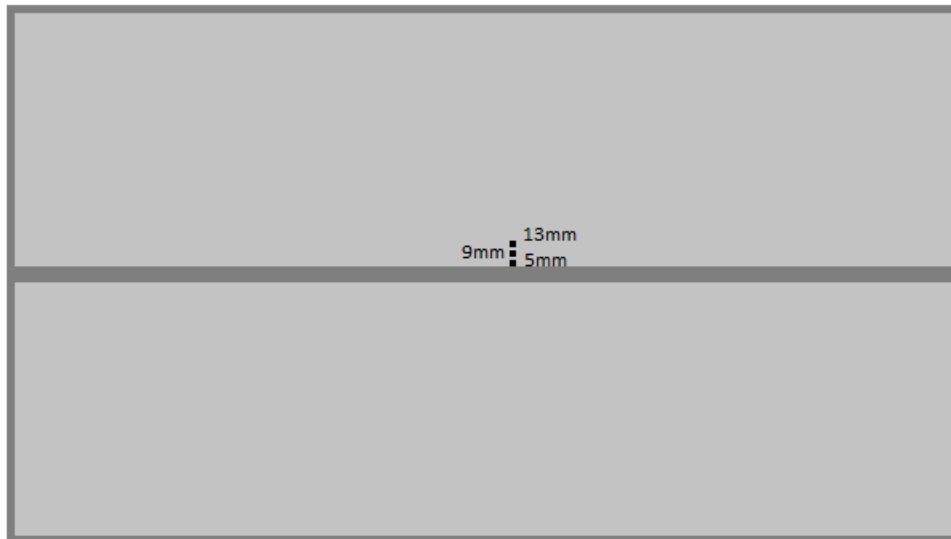


Figure 21: The position of all thermoelements used for FSW. The text in the figure tell the distance of the thermoelement from the weld centre

3.3.1 Welding parameters

Welding parameters used in the FSW experiments can be found in table 4. Since all the different plates are from the same material, it was natural that a lot of the parameters were kept the same. The only difference between the welds, was that a higher rotation speed was used for the T6

reference. The reason for this, is that this material was assumed to have a higher strength than the rest, meaning more energy would be required to make a deformation necessary for the FSW process to work. Only small differences were assumed in the hardness for the heated plates, making it possible to use identical parameters for all these.

Table 4: Welding parameters used in the FSW experiments.

Welding parameter	Plates heated to 430°C	T6 reference
Rotation speed [rpm]	1500	2000
Speed [mm/s]	6.3	6.3
Downforce [kg]	820	820
Peak at current [A]	7	7
Start delay [ms]	2000	2000
Acceleration [mm/s ²]	100	100
Rotation direction [CW/CCW]	CW	CW
Tilt [°]	3	3

3.3.2 Welding tool

When it comes to the welding tool, the same tool was used for all the welding experiments. The shoulder dimensions were based on the 6mm plate thickness (3.5 x thickness). From previous trails, this welding tool provided high strength defect free welds. Information of the welding tool is given in table 5. Figure 22 shows a picture of the welding tool.

Table 5: Information about the welding tool used in the friction stir welding experiments. Information is given about both the pin and the shoulder.

Pin				Shoulder	
Type	Diameter [mm]	Pin length [mm]	Plate thickness [mm]	Type	Diameter [mm]
Cylindrical finned	6	5.86	5.9	S1	20



Figure 22: A picture of the welding tool used in the friction stir welding experiments.

3.4 Metal Inert Gas Welding

Different MIG welding methods are described in section 2. The one used in this thesis is the SyncroPulse method. A frequency of 3.5 Hz was used in all the MIG welding experiments.

Five thermocouples were inserted in each plate, at the distances 5, 9, 13, 25 and 75mm from the weld centre. The thermocouple placed at a 75 mm distance from the weld centre was positioned at the end of the plate. The positioning of the thermocouples are given in figure 23.

Table 6: Welding parameters used in the MIG experiments. All parameters were kept the same for both welding except the current, which were 165A for the first weld and 185A for the second.

Welding parameter	Plates heated to 430°C	Plates heated to 550°C	T6 reference
Current [A]	165/185	165/185	165/185
Voltage [V]	20	20	20
Gross power [kW]	3.57	3.57	3.57
Welding speed [mm/s]	13	13	13

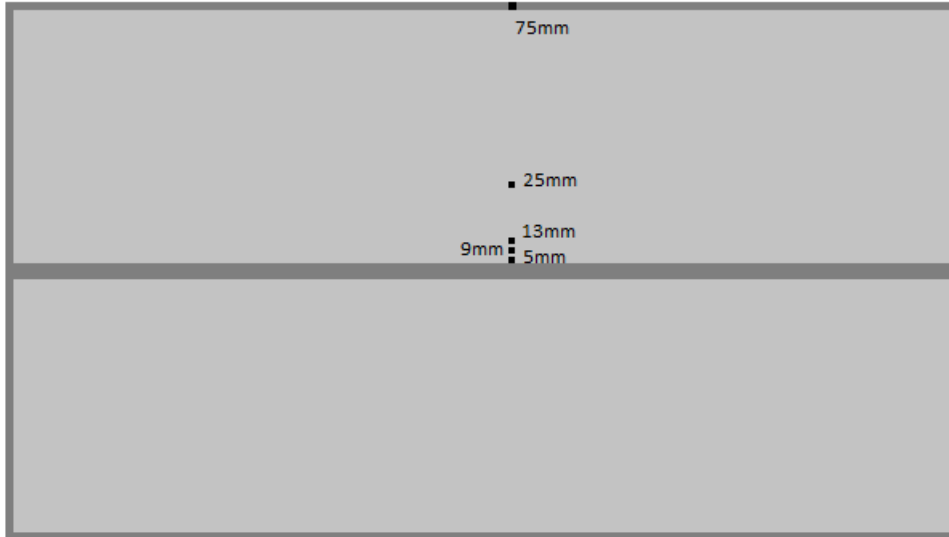


Figure 23: The position of all thermoelements used for MIG welding. The text in the figure tell the distance of the thermoelement from the weld centre.

The welding was done at SINTEF Industri. Seven different cases were welded. These are all the three cooling methods after heating to the two temperatures 430°C and 550°C, in addition to the reference T6-state.

For each of these welds, the plates were welded two times, one on each side. The welding direction was opposite for each of these welds. A higher current was used for the welding on the second side. All parameters from the welding experiment can be found in table 6.

The temperature was measured for both weldings of each plate for all seven different cases. This resulted in 14 total temperature measurements. These were later inserted into the simulation program NaMo.

3.5 Material Characterization

3.5.1 Grinding and Polishing

Smaller samples were cut from the cross section of each weld using a Discotom-5 watercooled saw. The blade was a 10S25 SiC cutting blade provided by Struers. Later, the samples were mounted in an Epofix cold-setting epoxy resin. Grinding and polishing were done at a Struers Tegramin-30 machine, and the different steps of this process is presented in table 7.

Table 7: The grinding and polishing steps.

Step	Surface	Lubricant	Time [min]	Force [N]
1	SIC FEPA #320	Water	3.5	30
2	SIC FEPA #1200	Water	10	30
3	MD-Largo	Diapro/Lar. $9\mu\text{m}$	7	30
4	MD-Mol	Diapro Mol $3\mu\text{m}$	12	50
5	MD-Nap	NAP-R $1\mu\text{m}$	15	50
6	MD-Chem	OP-U NonDry	15	50

The samples were rinsed with hot water and ultrasound between each step given in table 7. In addition, washing with soap, ethanol rinsing and blow drying were included after washing in ultrasound after the final step.

3.5.2 Optical Microscopy and Hardness Measurements

The samples were anodized in a mixture of 5% HBF_4 and 95% H_2O for 90 seconds. The potential for the anodizing was 20 V, and the maximum current 3 A. This was done to make the grain structure show.

The microscope used in this thesis was a Zeiss Axio Vert.A1 Inverted light microscope, with a magnification of 25.

The Vicker's hardness was measured using a Duramin-40 machine. One measurement was done on the top of the weld, and one measurement was done at the bottom, to show the difference between the different parts of the welds, if there are any. The distance between each measurement was 1mm. The machine used a force of 1kg, and a holding time of 10 seconds for each measurement.

The hardness measurements were compared to simulations done by NaMo. The simulations used the measured temperature from the cooling methods and welding processes as inputs. This means that the hardness was calculated only at the same positions as the temperature was measured during welding, resulting in a lot of hardness measurements and only a few simulated hardnesses.

3.6 Conductivity Measurements

The conductivity have been measured for all the plates at three different positions using a Sigmatest 2.069. When using this machine, a calibration first had to be made with two references with a conductivity of 4.4 MS/m (8% IACS) and 58 MS/m (100% IACS). A picture of the Sigmatest 2.069 is given in figure 24.



Figure 24: A picture of the Sigmatest 2.069.

The three positions where the conductivity were measured was at the end of the plates, 2-3 cm from the fusion line and right outside the fusion line. Five measurements were done per plate, and the plates were kept at room temperature during each measurement.

3.7 Tensile Testing

Tensile tests were done for all the samples described in this report. This includes two different heating temperatures, three different ways of cooling and two different welding techniques. Three samples were taken from each plate, resulting in a total of 42 tensile tests. These were all done at a MTS 810 testing machine. A picture from these tensile tests is given in figure 25.



Figure 25: A picture of the tensile testing process.

The dimensions of each specimen used in the tensile testing is given in figure 26.

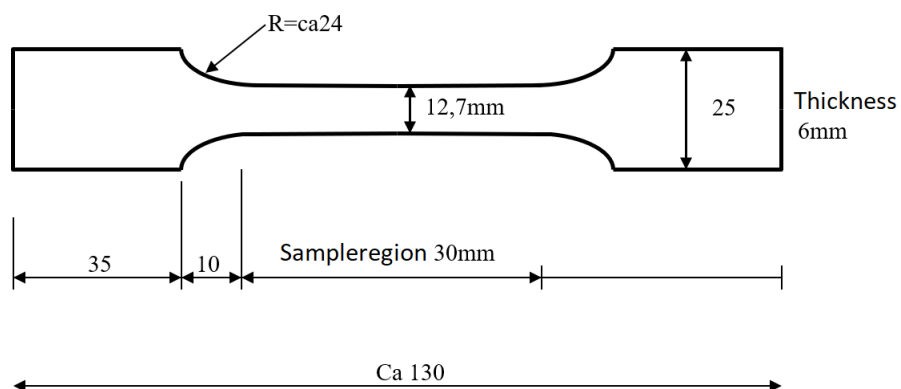


Figure 26: The dimensions of the specimens used in tensile testing.

After conducting the tensile tests, the results were compared to simulations done by NaMo. The issue here, is that NaMo calculates true stress and true strain, unlike the MTS 810 testing machine

that measures engineering stress and engineering strain. Therefore all the experimental data had to be converted into true stress and strain. This was done using equation ?? and ?? as described in section 2.

A note about the simulations done by NaMo is that the model has no understanding of necking or fracture yet. This results in infinite work hardening, something that definitely is not the case. Therefore it is a bit difficult to compare experimental data to simulated data. What is done, is that it is assumed that necking will start as the true stress from the measured data starts to decrease. This means that the output from NaMo has been compared to experimental data that first were converted to true stress and strain, to later only being drawn until the maximum stress value.

Over to the simulations, some explanation is necessary to understand how these were done. Since the mechanical properties depend on the distance from the weld centre, it is clear that it is impossible to give a perfect input to the NaMo model. Instead a choice has to be made for which part of the weld that should be used in the simulations. In this thesis, it is assumed that the region with the least hardness is the region that limits the tensile strength. Therefore the heat treatment of this region has been used as input for the simulations. From investigating the hardness test results, a minimum hardness value was found 9 mm from the weld centre for all cases, meaning that the measured temperatures in this point has been used as input for NaMo.

A note to be made, is that even though the temperature had not been measured at the same distance from the weld centre as the weakest point in the plate, it would have been possible to model the tensile strength using NaMo. It would only require an additional step of calculating the heat input for the NaMo model before the model can be used. A way of doing this is through the WTCP model described in section 2. This model is able to take welding parameters as an input and calculate the heat output in a metal plate at a given distance from the weld centre. Even though this model is made for arc welding, it can also be used for FSW, but then the temperature has to be measured at a given distance from the weld centre and the different welding parameters have to be calibrated until a similar temperature is both measured and calculated. In this thesis this step has been seen as unnecessary and therefore avoided. Still the model is described in section 2 as it could be used for similar problems, and it shows a more general solution to the problem.

4 Results

4.1 Grain structure

From light optical microscope investigations, pictures of the grain structure were taken. Most of these pictures are very similar, and therefore only the two best pictures are highlighted. These pictures are made large, so that it is easier to see the contrast between the grains. These are the grain structure of a FSW material (figure 27) and a MIG welded material heated to 550°C before welding (figure 28).

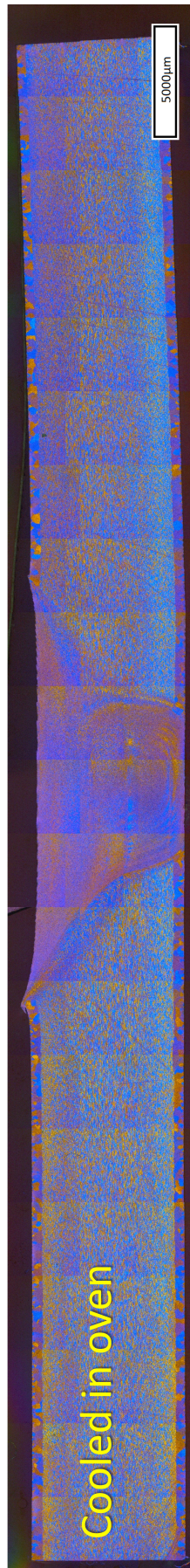


Figure 27: The grain structure of the FSW plate heated to 430°C and cooled in the oven.

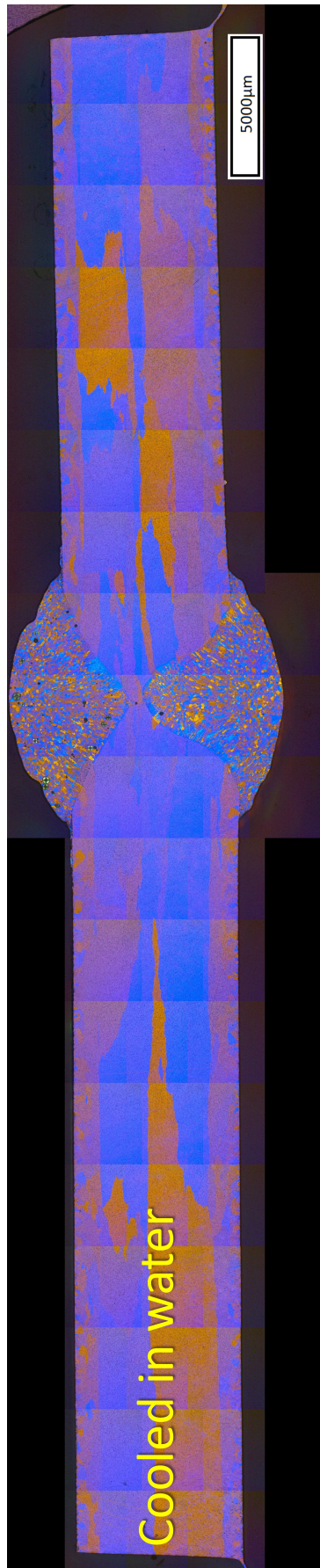


Figure 28: The grain structure of the MIG welded plate heated to 550°C and cooled in warm water.

Note that in addition to different welding techniques, figure 27 and 28 show material that was heated to different temperatures. This is important to remember when observing that the grain structure clearly is different also far from the weld for these figures.

It should also be mentioned that the grain structure clearly is different in the SZ and the FZ, compared to the base material. The welding has clearly had an impact on the grain structure.

A last note to figure 28, is that some black dots can be seen in the fusion zone.

Still, all experiments have been characterized in LOM. Figure 29 shows the grain structure of all the FSW plates, and figure 30 shows the grain structure of all MIG welded plates. These figures include all the different cooling methods in addition to the reference T6 state.

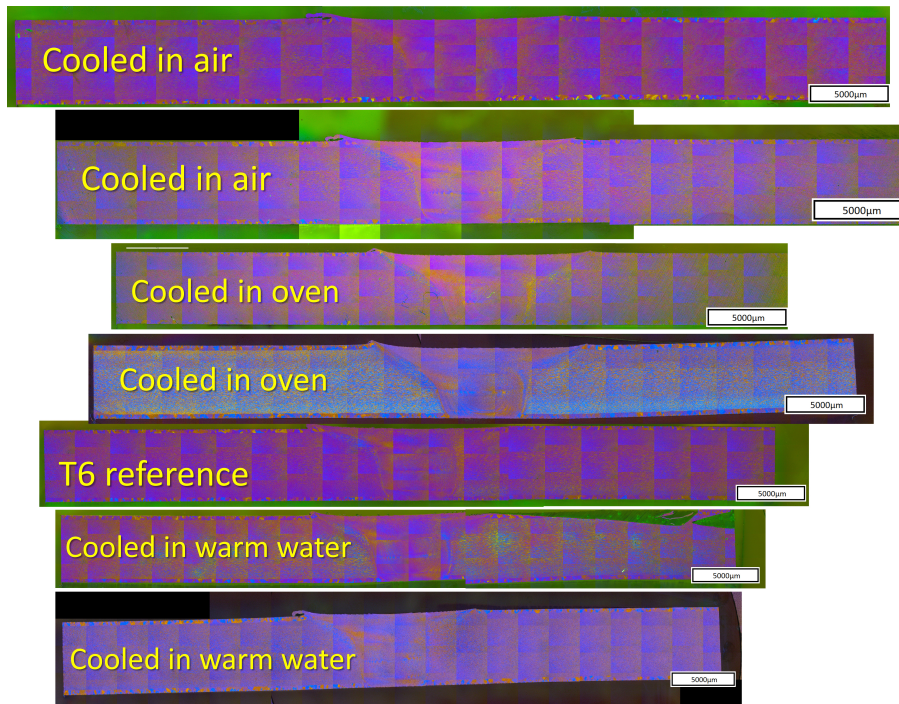


Figure 29: The grain structure of the FSW plates.

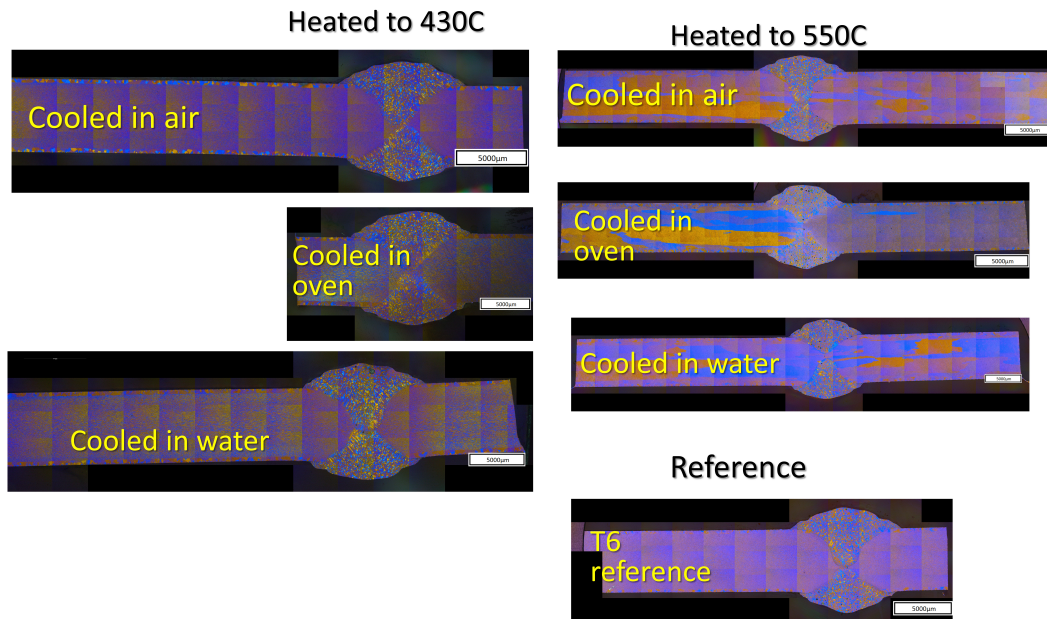


Figure 30: The grain structure of the MIG welded plates.

The observation that should be done from these two figures, is that the main difference between all grain structures are the welding technique and the heating temperature. Apart from these two things, all the grain structures seem to be similar. This indicates that the grain structure is independent on cooling method.

A second observation is that some pictures show a larger area of the plate than other pictures. This is simply because the grain structure is really the same for all cases, making it needless to report more than what is done here. To save time, only the necessary regions have been photographed for some samples, while the entire samples have been taken photo of for other samples. This is therefore only a choice made in the characterization process, and not a characteristic of the plates.

Black dots can be seen in multiple of the pictures of the MIG welded plates, given in figure 30.

4.2 Hardness

As described in section 3, hardness measurements were done across the weld for all the different experiments. Since this means a lot of measurements, they are presented in three different figures, separating each of the welding techniques as well as the heating temperature. The lines show the measured values, while the single dots show the result from simulations done by NaMo. These three figures are given as figure 31, 32 and 33.

Hardness of friction stir welded alloy that was heated to 433°C
(with both measured and simulated data)

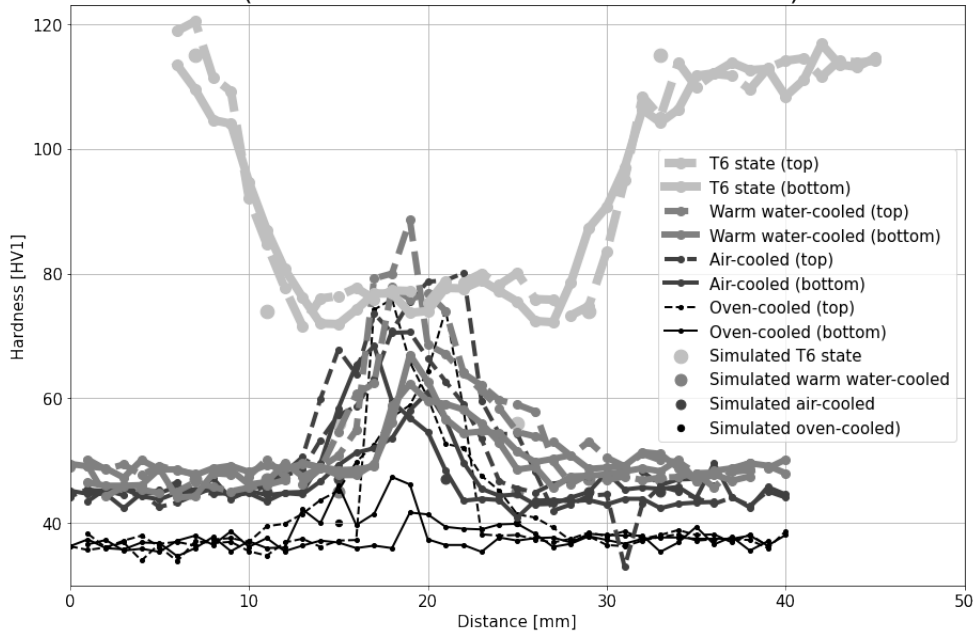


Figure 31: The hardness of all the FSW plates

Hardness of metal inert gas welded alloy that was heated to 433°C
(with both measured and simulated data)

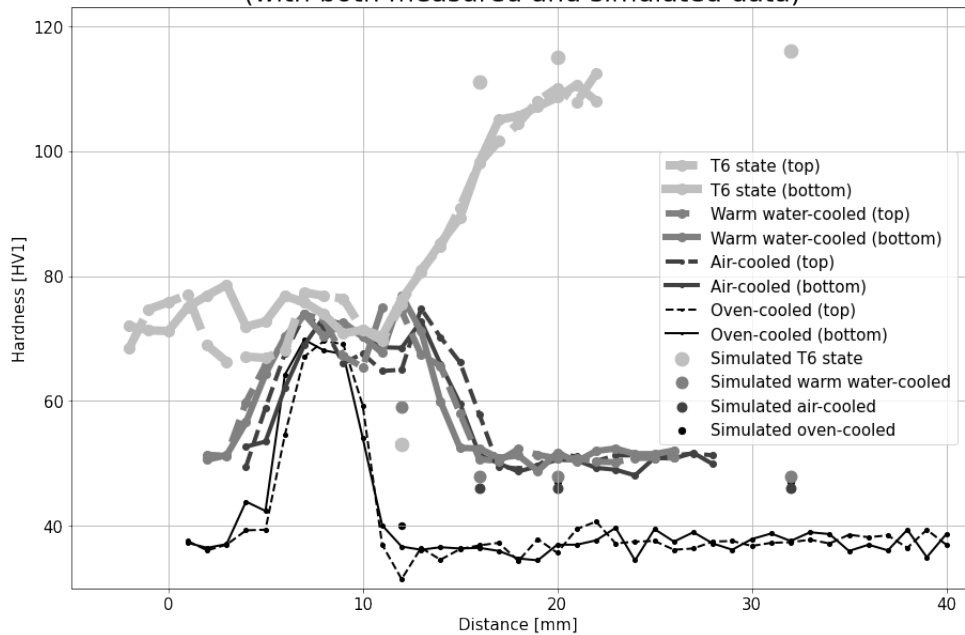


Figure 32: The hardness of all the MIG plates heated to 430°C

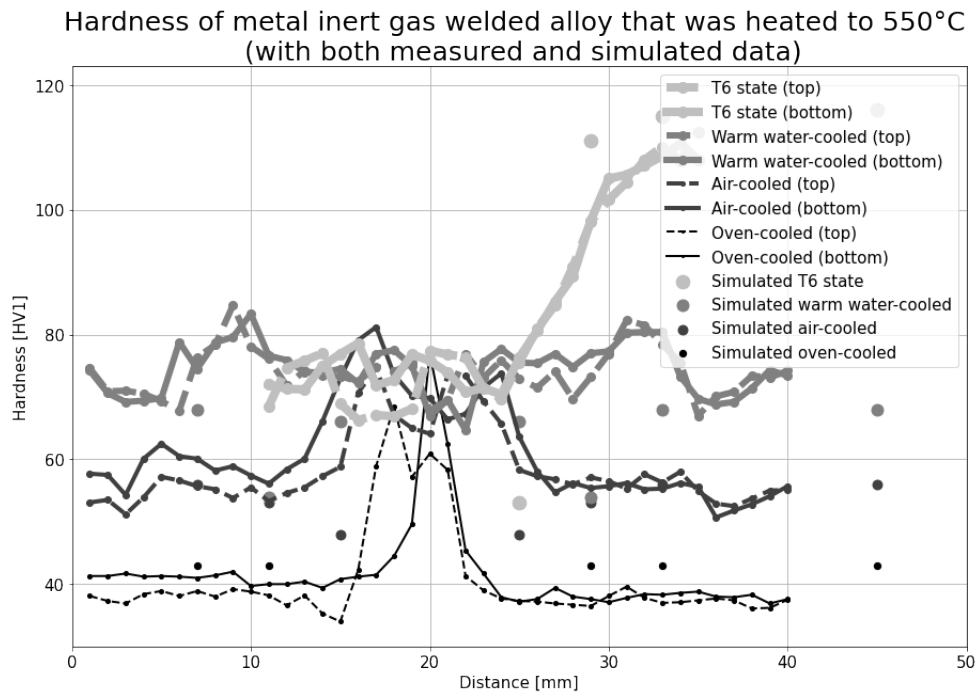


Figure 33: The hardness of all the MIG plates heated to 550°C

When it comes to what information the measurements can give, there are some observations that should be done. First off, it is clear that the reference state has the highest base material strength for all measurements, and that faster cooling rates lead to a higher base material strength. All the three figures show the same tendency where the reference state is hardest followed by warm water cooling, then air cooling and cooling in oven as the softest option.

As a second observation, it can be seen that the hardness also in the SZ decreases as the cooling time increases for the FSW. For MIG-welding, on the other hand, the hardness in the FZ is independent of the initial cooling time.

A third property of these welds, is that the dimension of the HAZ decreases when cooled slower. This is the same for all the different welds and heating experiments.

A fourth observation, is that a higher heating temperature results in a higher hardness, as the plates warmed to 550°C has a higher hardness than the plates heated to 430°C. This can be seen in figure 33. In addition, the difference between cooling in warm water, air and oven is more significant for this case. It should also be made clear that the plate that was heated to 550°C, and later cooled in warm water is the only result where the base material strength is similar to the weakest point in the reference.

One note to be made about these figures, is that the one showing MIG welding after heating to 430°C (figure 32) only shows hardness measurements on the right hand side of the weld, instead of showing the hardness on both sides, as is done in the other figures (figure 31 and 33). In addition, the hardness of the T6 reference for MIG heated to 550°C (figure 33) has only been measured on the right hand side. This has nothing to do with the plates, and is only a choice done to save time. The other cases have been measured on both sides of the weld, and no significant difference can be seen between the sides. Therefore it is assumed no significant difference would have been found for the MIG welded plate after heating to 430°C either.

4.3 Conductivity

The conductivity measurements are given in figure 34, 35 and 36. These figures show both the position and the value of all measurements.

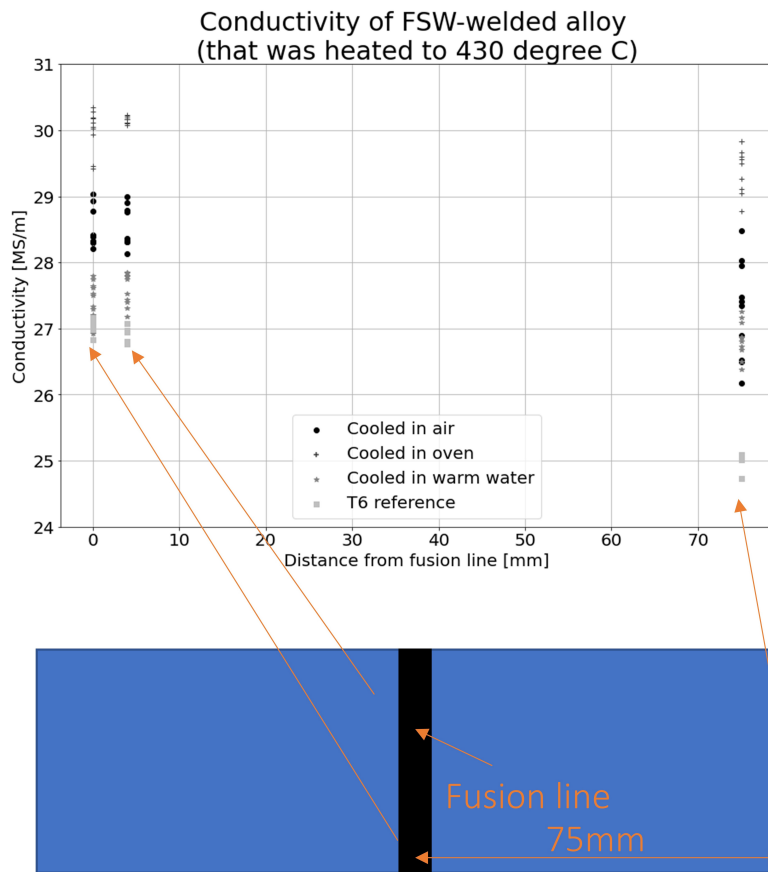


Figure 34: The conductivity of all the FSW plates heated to 430°C.

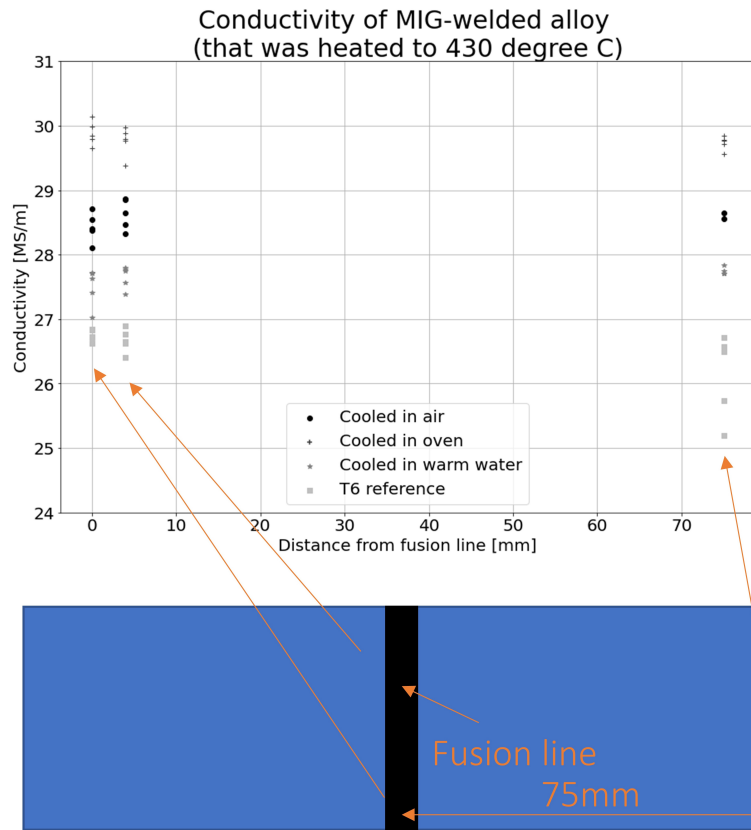


Figure 35: The conductivity of all the MIG plates heated to 430°C.

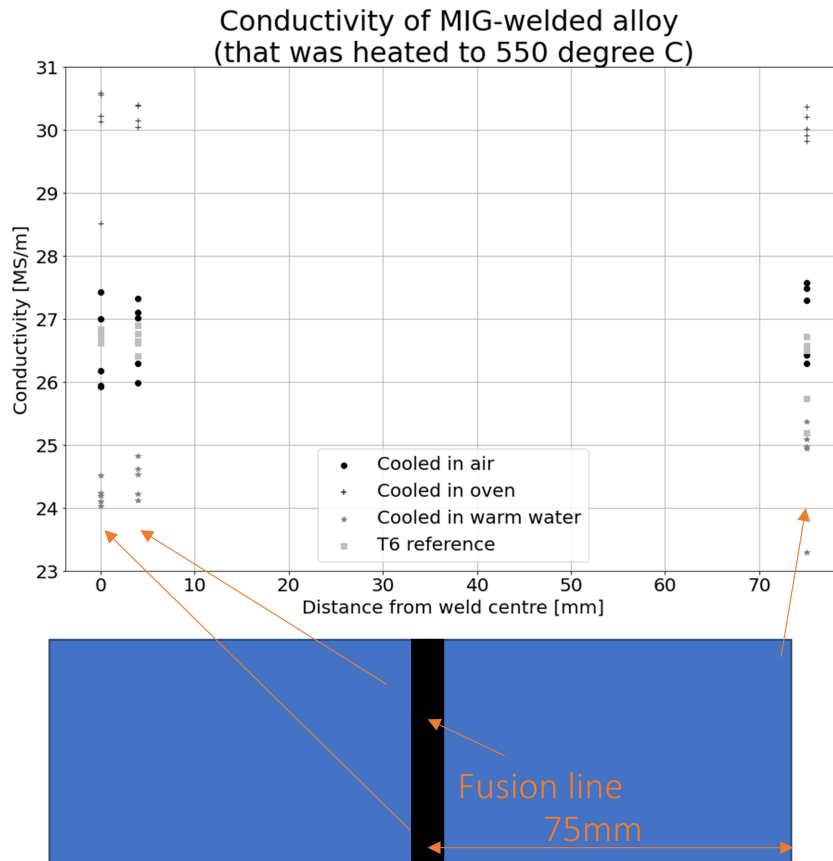


Figure 36: The conductivity of all the MIG plates heated to 550°C.

A note from the conductivity measurements, is that slower cooling results in higher conductivity. This is similar for all cases. It is also clear that the T6 reference has the lowest conductivity.

Another note is that the conductivity is relatively similar for all distances from the fusion line. There is some decrease as the distance increases, but this difference is small compared to the difference between each cooling method. Therefore it seems valid to assume cooling time has a larger impact on conductivity than the distance from the fusion line.

In addition, the conductivity is relatively similar between both the plates that was FSW and the plates that was MIG welded after being heated to 430°C. Therefore it can be assumed that also welding technique has a small impact on conductivity.

Lastly, it can be seen that the case were the conductivity is quite different is for the case were the material was heated to 550°C, and later MIG welded, compared to plates being heated only to 430°C before welding. This indicates that heating temperature has a significant impact on conductivity, in addition to the cooling time, as previously mentioned.

4.4 Tensile test

After conducting tensile tests and comparing these to simulations, a lot of graphs were obtained. Since there were so many results, the results from the tensile tests are split into three figures, one figure for each of the different welding experiments. These figures show both experimental data and simulated data from NaMo. The dashed lines are what is simulated. The tensile test results from each welding are presented in figure 37, 38 and 39.

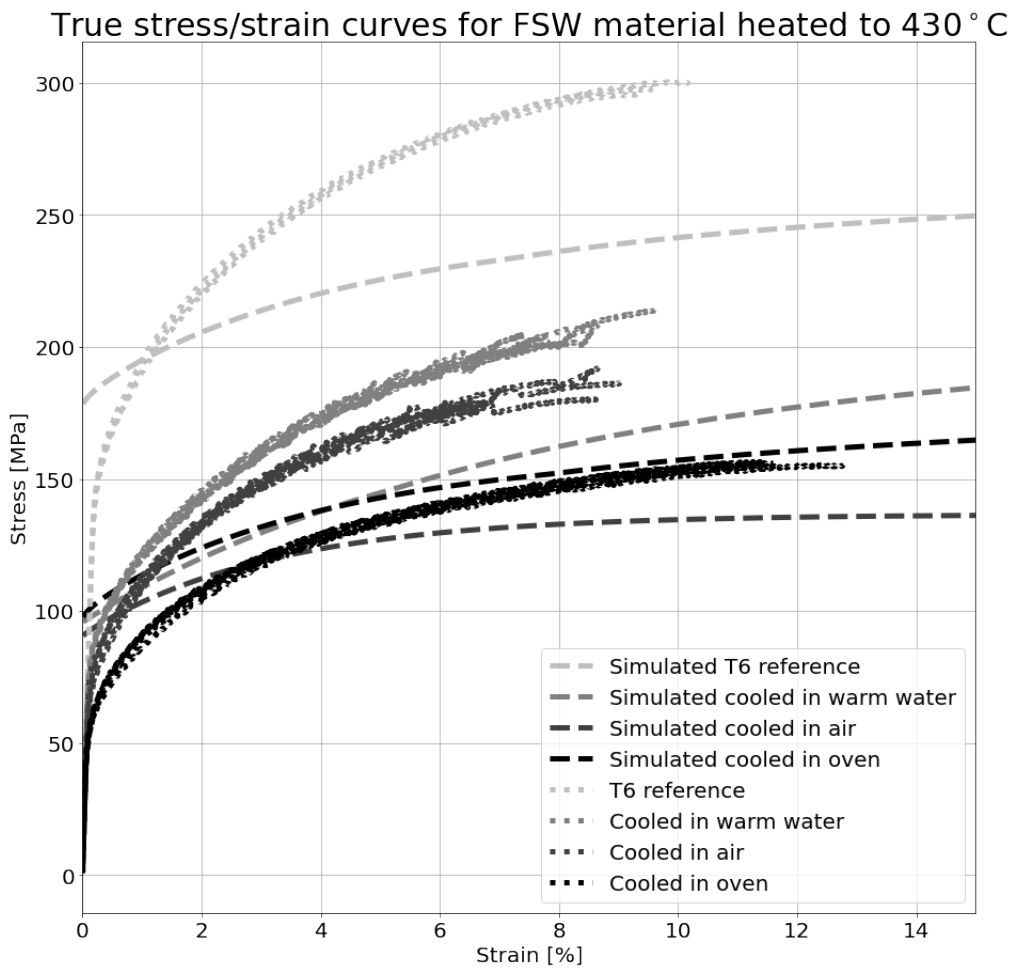


Figure 37: The conductivity of all the MIG plates heated to 550°C.

True stress/strain curves for MIG welded material heated to 430 ° C

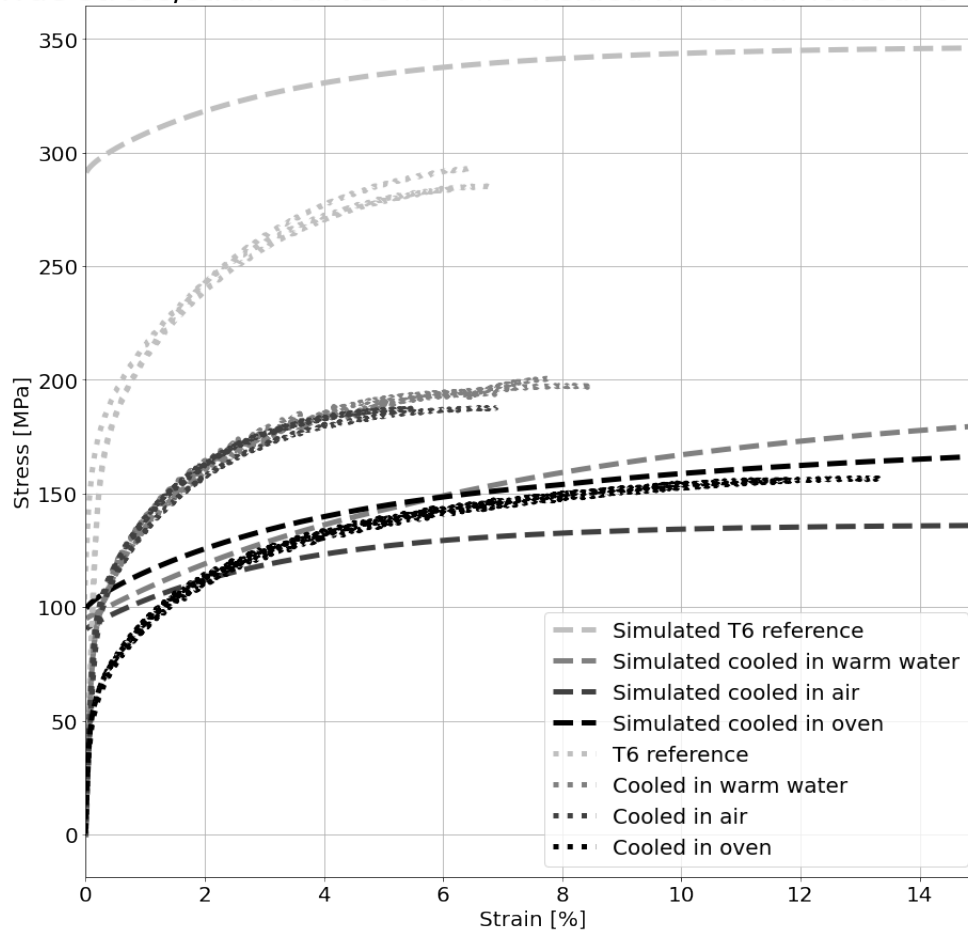


Figure 38: The conductivity of all the MIG plates heated to 550°C.

True stress/strain curves MIG welded material heated to 550 °C

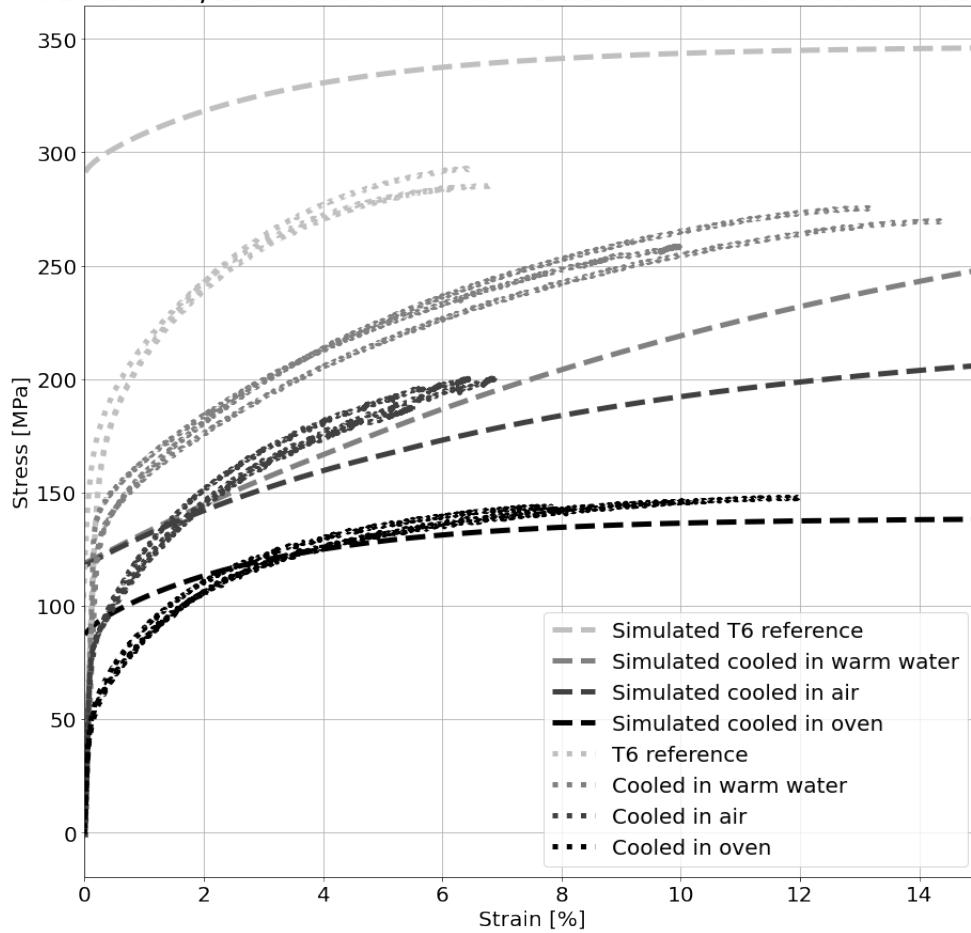


Figure 39: The conductivity of all the MIG plates heated to 550°C.

From these graphs it is possible to see that the reference T6 state alloy has a higher strength than the rest. When considering the cooling time, it seems faster cooling leads to an increased tensile strength. This is the case for all the figures.

Another observation that should be made, is that the simulated values gives a lower stress at the same strain than the experimental data for FSW. For MIG welding, on the other hand, the simulations show a higher stress value than what is measured. This means that welding procedure clearly has an impact on how the model is able to describe the process.

Lastly, the different figures should be compared. It is then clear that the material experiencing FSW has a slightly higher tensile strength than the plates that was MIG welded. It also seems a higher heating temperature leads to a higher tensile strength when comparing the two different MIG welding experiments.

5 Discussion

5.1 The Microstructure in the Base Material

From section 4, it seems like slower cooling methods lead to less strength in Al-Si-Mg alloys. This can be seen from both the hardness tests and the tensile tests.

In section 2 it is explained that to get high strength for Al-Si-Mg alloys, what is important is to get the correct microstructure. The preferred precipitates are the needle shaped β'' particles. β' and β particles will not contribute to high strength, making a softer material, were β has the least strength contribution of the two.

It could naturally be assumed that there is a higher concentration of β'' particles in the alloy were the strength is higher, compared to metals with less strength. In fact the difference in strength in the base material is so significant when comparing the reference alloy to the alloys cooled in oven, that there probably is a lot of strength contribution from precipitates such as β'' in the reference alloy and none in the slower cooled metals. For the slower cooled alloys, the strength is so much lower that it seems almost like no strength contribution from precipitates can be found in the metals, leading to a high probability that the microstructure consists of mostly β . This makes the slowly cooled metals overaged.

Further assumptions can be made about the microstructure in the base material, also for the other cooling methods. The summary of these assumptions is given in table 8 and 9, showing the microstructure of the base materials for the two different heating temperatures.

Table 8: The most likely microstructure in the base material for each cooling method after heating to 430°C

Cooling method	Microstructure
Cooled in oven	β
Cooled in air	β
Cooled in warm water	β' and β
Reference	β''

Table 9: The most likely microstructure in the base material for each cooling method after heating to 550°C

Cooling method	Microstructure
Cooled in oven	β
Cooled in air	β' and β
Cooled in warm water	β'' and β'
Reference	β''

It should be noted that the microstructure given in table 8 and 9 is only based on the hardness tests, and cannot be taken as a given fact. It could be possible to determine the exact microstructure for each case, but that would require SEM analysis, which has not been done in this thesis. Still, a qualitative guess of the microstructure is probably quite right, and can at least give some understanding of how the properties of the different cases has emerged.

Something clear is that slow cooling gives more equilibrium, β , particles. This can be explained by the precipitation hardening sequence presented in section 2. There it was written that the SSSS phase is a necessity for gaining any precipitation hardening during aging. This phase arises when the metal is quenched after SHT. Most of the cooling methods are very slow, meaning that there is no quenching. This then means that Si and Mg atoms will dissolve from the solid solution during the cooling. At high temperatures, the diffusion will be very high, making the phase transformation to the equilibrium phase very fast. Therefore it would be natural to assume that the microstructure consists of mostly equilibrium phase, β . The structure is overaged, and low strength is a given.

The conductivity measurements support the assumption that there is mostly β particles for the cases with slow cooling. In section 4 it can clearly be seen that there is a higher conductivity for the cases with fast cooling than when the cooling is low. As explained in section 2, this means that less alloying elements are in the solid solution, making a relatively pure Al matrix with some particles consisting of Si and Mg. For the cases where the conductivity is low, there are more elements in the solid solution, resulting in a less pure Al matrix.

A last note about the microstructure in the base material of the Al-Si-Mg alloys considered in this thesis, is that clearly 550°C is a temperature high enough to initiate grain growth and recrystallization, while 430°C is too cold.

5.2 Properties of the Weld Zones

In section 4, it was observed that a slower cooling rate leads to a thinner HAZ. This indicates that there are some differences in the microstructure originating from the heat treatment, affecting how the mechanical properties end up after welding.

It is already made clear that the base material of the slowly cooled plates consist of mostly β phase, in contrast to the faster cooled plates that has a mix of β'' and β' . For the plates with a mix of β'' and β' precipitates, high welding temperatures will result in the particles reacting into more β phase, resulting in a hardness decrease. This reaction will then happen at a relatively large area due to the fact that β'' particles are very unstable at high temperatures. When a microstructure of β is heated, on the other hand, the microstructure is already at the equilibrium, making it impossible for any reaction to happen. Still, the hardness does change close to the weld centre, even though the microstructure consists of mostly β . This is because the temperatures are high enough to make the particles go into solid solution and then restart the precipitation process. This makes it possible to get some β'' , even though the initial composition consisted of mostly β . This restart of the precipitation process happens at a shorter distance from the weld centre than formation of β' from β'' , due to the fact that higher temperatures are needed to make β particles unstable and go into the solid solution. This explains how slower cooling rates lead to more β , and then a shorter HAZ, compared to faster cooling rates that result in β'' and a longer HAZ.

In addition, some differences can be seen in the weld zones between the two different welding techniques. This is documented in the LOM pictures given as figure 29-30 in section 4. Firstly, it should be mentioned that pictures of the FSW are more flat in the weld zone than the MIG welded plates. This is due to the fact that MIG welding introduces new material, that makes the weld zone thicker, unlike FSW that does not add any new material. When considering that the aim of this thesis is to find a welding technique suited for constructions, a point should be made that having welded plates without any added thickness should be seen as an advantage.

More importantly, pictures of the grain structure show how there is a significant difference between the different zones of the weld. There is clear that a lot has happened to the microstructure during the welding process. To give a short answer, what can be seen is what is described as normal for these welding techniques in section 2. This means that the welds are of a good quality, and that the welding parameters described in section 3 results in good quality welds.

There is one aspect of the WZ, however, that rises a minor concern. In both figure 28 and 30, some small black circles can be seen inside the fusion zone for the MIG welded plates. These dots are what is called pores, and they are parts of the weld where there is no metal. This is something that happens during welding if gas is trapped inside the metal, and does not escape before solidification. To get a perfect weld, an effort should be made to get rid of all these pores. Still, during both hardness testing and tensile testing, it was shown that the weakest point of the welds were in the HAZ and not in the FZ. Therefore the pores does not have a large enough negative impact on the mechanical properties to be the limiting factor when dimensioning the metal.

5.3 The Preciseness of the NaMo model

Based on the results in section 4, it is possible to tell something about the preciseness of the simulation model NaMo. This model has been compared to both hardness tests and tensile tests, giving a clear picture of how well the model is able to predict these phenomena.

Starting with the hardness tests, what can be observed is that the model struggles to describe what happens for a Al-Si-Mg alloy close to the weld centre. This is the case for both welding methods. This can be explained by the fact that the NaMo model is limited to only calculate what happens to the microstructure of Al-Si-Mg alloys and the resulting hardness based on a heat input or on plastic strain. The nature of FSW and MIG welding is not included in the model, making it expected that the model would fail to calculate a correct microstructure close to the weld centre. The model should not be able to calculate what happens at positions where extreme plastic deformation or adding of new material has happened.

Further from the weld centre, the model is able to give a reasonable good approximation of the hardness. Simple calculations give an error of only 6% when an average was taken for all hardness measurements at distances above 5mm from the weld centre. This means that the model is able to predict how Al-Si-Mg alloys react to thermomechanically processing. NaMo is able to predict an accurate hardness when only temperature is the input. This means that the model works for the cases where it would be expected to work as well.

The tensile tests are different. Here, the model seems to have some problems agreeing to experimental data. It is already observed in section 4 that the model predicts a lower strength than what is measured for FSW, while the opposite is true for MIG welding. There could be multiple reasons why this is the case.

Firstly, it should be mentioned that something could be off with the assumptions described in section 3. It could be that the transformation from engineering stress-strain to true stress strain has an impact on the result, shifting the shape of the experimental graphs.

Secondly, it should be made clear that the tensile strength are measured above the welds. Therefore the strength of the welds could definitely have an impact on the final result. In section 3 it was assumed that most elongation happened in the region of least strength, and that this strength is what determined the shape of the curves. In reality the strength depends on the distance from the weld centre, making it a complex task to predict exactly how much the metal is able to elongate before fracture. Especially when there is a large area with relatively similar hardness, it can be expected that some elongation and work hardening also will happen in regions of slightly larger strength too. This will then lead to different results than what the model assumes, which is a sample without any differences in tensile strength.

The fact that the model predicts a too low strength for FSW and a too high strength for MIG, indicates that some elongation must have happened also in the weld zone. So, why is there a difference in what happens for the two different welding techniques? A clear difference between them is that FSW gives a lot of deformation in the weld zone, while MIG only introduces a new metal. From the hardness tests described in section 4, it is possible to see that the FSW plates have a hardness above 80 HV1 at the weld centre, while the hardness of the MIG welded plates is below 80 HV1 at the same position. This means that the added metal for MIG has a lower strength than the deformed metal after FSW. This difference is probably the reason for why the model fail to describe the relationship between stress and strain in opposite directions for the two different welding techniques.

Thirdly, the values for strain from the experimental data should be taken with a grain of salt. From the experimental setup described in section 3, it is clear that only extensions between two points are measured. All extensions outside of these points will therefore not be included in the graphs. Normally this would not be a problem since these points are in a thinner region of the sample, and the assumption that nearly all extension happens here is almost entirely valid. The problem with these experiments, is that the properties vary with the distance from the weld centre. This may lead to the graphs showing less extension than what is actually the case in the experiments. If this is the case, all experimental graphs should be shifted more to the right, and if this would happen,

they would also match the calculations from NaMo better.

The problem with this argument, is that it proves how the graphs showing true stress-strain has little value. The main information from the figures is the point showing maximum strength before fracture. This is very good to know, to get an understanding of the maximum strength the alloy have, but it is very little useful when comparing it with NaMo. Since the model has no understanding of necking or fracture, it assumes work hardening will continue forever, meaning that no maximum value will ever be found. This means it is really not possible to tell how accurate the model describes the tensile strength for the experiments conducted in this thesis.

5.4 Which Cooling Method and Welding Technique is the Best?

As stated in section 1, the goal of this thesis is to produce large profiles of aluminium with similar properties as traditional production, but at a lower cost. This then means that the economy aspect also should have its impact on the choice of welding technique.

Firstly, MIG welding needs more processing steps before welding is possible than FSW needs. This includes the oxide layer at the surface of the aluminium that must be removed for MIG and not for FSW, making FSW preferred. In addition the X-shaped surface used for MIG welding in this thesis is more complex than the I-shaped surface used for FSW.

In addition the added material in MIG welding will increase the cost, compared to FSW were no material is added. Another point is that since there is only one alloy in the final product, FSW materials will be easier to recycle, making the process more sustainable.

The welding time itself is quite similar between the two methods, but in this thesis the MIG welding was done twice (on both sides of the plate). Therefore the welding time ended up almost the double for MIG compared to FSW.

Lastly, the cost of a protective atmosphere is another disadvantage with MIG welding. When compared with FSW, this is an additional cost, since FSW does not need this.

When considering other factors than prize, it is shown that FSW only leaves small extensions to the welded profiles. In section 4, it can be seen how arc welding leads to a local increment of the thickness of the plates. This non-flat geometry can potentially lead to problems, and should therefore be avoided if possible.

When it comes to the mechanical properties, FSW has a higher hardness in the weld zone than MIG has, as previously mentioned. This is due to deformation of already existing material instead of introducing new material.

When considering tensile strength, it can be seen that FSW has a higher maximum strength than MIG after heating to the same temperature. Therefore it seems FSW gives a higher overall strength.

When considering cooling methods, two observations were made in section 4. Firstly, an initial heating temperature of 550°C gives a much higher strength than heating to 430°C. Secondly, faster cooling leads to higher strength. The only experiment in this thesis that proved a promising result was when the plates were cooled in warm water. All other experiments, except the references, had a base material strength below the strength in the weld and will therefore not be suitable for applications this thesis is trying to find good welds for. Therefore it seems only warm water cooling is the only useful result from this thesis.

6 Conclusions

Based on the discussion in section 5, some conclusions can be made. These include the most likely microstructure resulting from each cooling method in the base material, why the properties of the weld zones are as they are, how precise the NaMo model is and which cooling method and welding technique is the best of all that were tested.

So, as a beginning it seems slower cooling rates lead to higher concentrations of β particles in the material. In addition, this concentration is even higher when the metal is only heated to 430°C than when heating to 550°C. This is because longer times at higher temperatures make most of the structure to consist of the equilibrium phase, β . The β particle gives only a small strength contribution to the alloy, resulting in a soft metal.

The weld zones have are of a similar nature to what could be expected from the theory described in section 2. In addition slower cooling methods lead to thinner HAZs as a result of more β particles in the base material. These particles will be stable up to high temperatures, meaning that changes in the microstructure only will happen close to the weld centre. When the metal has more β'' and β' lower temperatures are required to make β particles, meaning that the HAZ will be larger. Some small pores were found from the MIG welds, indicating that the welding parameters could be changed if similar welding would be done in the future.

When it comes to the NaMo model, this seems to give good predictions for the experiments described in this thesis. When comparing the hardness, the model worked fine for calculating the hardness in the base material with only an error of 6%. Closer to the weld centre, the model struggled due to the fact that the model is not programmed to understand either FSW or MIG. For the tensile strength, the model had more problems. Since there is no way the model is able to understand necking and fracture, it is hard to compare the results between the model and the experimental tests, especially when there is a lot of uncertainty about how accurately the elongation measurement really is valid for the tests.

It is clear that the best welding technique is FSW, and that the best cooling method is cooling in warm water after heating to 550°C. Therefore it is natural to assume that combining these will give the best result. This has not been done in this thesis, so if this indeed is the case, is something that should be validated in further work. Still this is what all the results point towards. All the other experiments result in a significantly softer material than the reference T6 alloys.

One last mention is that even though warm water cooling seems promising, it is clear that it might not be the only possible solution to the problem described in section 1. It could well be that strengthening the HAZ with increased material or some clever geometry is still the best option for a lot of cases.

7 Further Work

As a starting point for this section, it should be made clear that this thesis only focused on what can be described as a starting point for further investigations. This means that a lot can be put into further work.

As a start, most of the experiments fail to give any meaningful answer to the aim of the thesis. The only promising result is cooling in warm water from a temperature of 550°C. All the other results are really only giving so bad results that the only point of them is to show how not to heat treat Al-Si-Mg alloys. Therefore it is natural to assume that optimization of heating to 550°C followed by warm water cooling and FSW can result in increased strength in the metal. In addition it should be mentioned that this experiment has not even been conducted, making it natural to validate this assumption as the next step in this investigation.

Further, it could be natural to change the parameters slightly if further work were to happen. One possibility is that warm water cooling work better if the temperature in the water is something different than 90°C. Maybe 50°C is the perfect temperature, maybe 70? One way of determining this, is by using the NaMo model. This model has in this work proved to be able to describe this type of thermomechanical processing with a low error. Therefore it is natural that this could be used in the optimization process in the future. This would make it possible to make more qualitative guesses of thermal treatment for the alloys, so that all the experiments have a purpose, unlike most of the experiments in this thesis that only proved how not to heat treat Al-Si-Mg alloys.

In addition, only one set of welding parameters have been investigated. It could be that changing the pressure or the welding speed during FSW will make a better weld.

Also it could be possible to look into other properties of the Al-Si-Mg alloy than only hardness and tensile strength. For example corrosion resistance could be of interest, and should be taken into account depending on the situation.

If further verification of the results in this thesis were to be considered, transmission electron microscope (TEM) analysis could be able to spot the precipitates in the Al-Si-Mg alloy. Therefore these investigations could be considered doing in the future.

When considering sustainability, it is natural to assume the solution proposed in this thesis is a good choice. By avoiding any complicated geometries or added structures to strengthening the HAZ after welding, the aluminium alloy maintain the same purity also after melting and recycling, as no non-aluminium structures are added. Still, the recycling process of Al-Si-Mg alloys has not been investigated in this thesis, and is a natural next step for further work.

Lastly, it is clear that the NaMo model has a good understanding of Al-Si-Mg alloys. It can with good accuracy describe a lot of processes. Still, it is hard to draw any conclusions from the tensile measurements done in this thesis due to how the model cannot describe necking, fracture or welding. Therefore if some of these mechanics had been included in the model, it would make even more useful than it is today.

References

- [1] H. B. Aaron, D. Fainstein, and G. R. Kotler. Diffusion-limited phase transformations: a comparison and critical evaluation of the mathematical approximations. *Journal of applied physics*, 41(11):4404–4410, 1970.
- [2] H. Aaronson, C. Laird, and K. Kinsman. Phase transformations. *ASM, Metals Park, OH*, 313, 1970.
- [3] A. Ajri and Y. C. Shin. Investigation on the effects of process parameters on defect formation in friction stir welded samples via predictive numerical modeling and experiments. *Journal of Manufacturing Science and Engineering*, 139(11), 2017.
- [4] A. Bahrami. Modeling of precipitation sequence and ageing kinetics in al-mg-si alloys. *Sharif University of Technology, Tehran*, 2010.
- [5] D. Bajić. Postupci zavarivanja. *Univerzitet Crne Gore, Mašinski fakultet, Podgorica*, 2014.
- [6] J. Banhart, C. S. T. Chang, Z. Liang, N. Wanderka, M. D. Lay, and A. J. Hill. Natural aging in al-mg-si alloys—a process of unexpected complexity. *Advanced engineering materials*, 12(7):559–571, 2010.
- [7] Y. Bergström and H. Hallén. An improved dislocation model for the stress-strain behaviour of polycrystalline α -fe. *Materials Science and Engineering*, 55(1):49–61, 1982.
- [8] D. Bratland, Ø. Grong, H. Shercliff, O. Myhr, and S. Tjøtta. Overview no. 124 modelling of precipitation reactions in industrial processing. *Acta Materialia*, 45(1):1–22, 1997.
- [9] A. V. Bugten. Possibilities of improving the structural properties of welded al-mg-si alloys through automated local induction heat treatments. Master’s thesis, NTNU, 2021.
- [10] L. Cao, P. A. Rometsch, and M. J. Couper. Clustering behaviour in an al–mg–si–cu alloy during natural ageing and subsequent under-ageing. *Materials Science and Engineering: A*, 559:257–261, 2013.
- [11] J. R. Davis et al. *Aluminum and aluminum alloys*. ASM international, 1993.
- [12] A. Deschamps, Y. Bréchet, and F. Livet. Influence of copper addition on precipitation kinetics and hardening in al–zn–mg alloy. *Materials Science and Technology*, 15(9):993–1000, 1999.
- [13] S. Dev, B. Murty, and K. Rao. Effects of base and filler chemistry and weld techniques on equiaxed zone formation in al–zn–mg alloy welds. *Science and Technology of Welding and Joining*, 13(7):598–606, 2008.
- [14] C. ed Kammer. *Aluminium Handbook; Vol. 1: Fundamentals and Materials*. Aluminium-Verlag Marketing and Kommunikation GmbH, 1999.
- [15] G. Edwards, K. Stiller, G. Dunlop, and M. Couper. The precipitation sequence in al–mg–si alloys. *Acta materialia*, 46(11):3893–3904, 1998.
- [16] V. Fallah, A. Korinek, N. Ofori-Opoku, B. Raeisnia, M. Gallerneault, N. Provatas, and S. Esmaeili. Atomic-scale pathway of early-stage precipitation in al–mg–si alloys. *Acta materialia*, 82:457–467, 2015.
- [17] I. Faridmehr, M. H. Osman, A. B. Adnan, A. F. Nejad, R. Hodjati, and M. Azimi. Correlation between engineering stress-strain and true stress-strain curve. *American Journal of Civil Engineering and Architecture*, 2(1):53–59, 2014.
- [18] F. Fazeli, C. Sinclair, and T. Bastow. The role of excess vacancies on precipitation kinetics in an al-mg-sc alloy. *Metallurgical and Materials Transactions A*, 39(10):2297–2305, 2008.
- [19] J. Friedel. *Dislocations: international series of monographs on solid state physics*, volume 3. Elsevier, 2013.

-
- [20] H. FROST and M. ASHBY. Deformation-mechanism maps: The plasticity and creep of metals and ceramics(book). *Oxford, Pergamon Press, 1982, 175 p*, 1982.
- [21] T. Furu, O. Ryen, and O. Myhr. Effect of pre-deformation on age hardening kinetics in commercial 6xxx alloys. In *Proc. 11th Intern. Conf. Aluminium Alloys*, pages 1626–1633, 2008.
- [22] V. GEROLD. Precipitation hardening. *Dislocations in solids*, (4), 1979.
- [23] Ø. Grong. Sveisemetallurgi, 1990.
- [24] Ø. GRONG. Recent advances in solid-state joining of aluminum. *Welding journal*, 91(1): 26–33, 2012.
- [25] Ø. Grong and D. Grong. *Metallurgical modelling of welding*, volume 2. Institute of materials London, 1997.
- [26] A. Hamarsnes. Mechanical properties of a welded 6082 aluminium alloy with local heat treatments. Master’s thesis, NTNU, 2019.
- [27] H. S. Hasting, A. G. Frøseth, S. J. Andersen, R. Vissers, J. C. Walmsley, C. D. Marioara, F. Danoix, W. Lefebvre, and R. Holmestad. Composition of β precipitates in al–mg–si alloys by atom probe tomography and first principles calculations. *Journal of Applied Physics*, 106 (12):123527, 2009.
- [28] R. Kampmann, H. Eckerlebe, and R. Wagner. Precipitation kinetics in metastable solid solutions—theoretical considerations and application to cu-ti alloys. *MRS Online Proceedings Library (OPL)*, 57, 1985.
- [29] U. Kocks. A statistical theory of flow stress and work-hardening. *Philosophical Magazine*, 13 (123):541–566, 1966.
- [30] U. Kocks. Laws for work-hardening and low-temperature creep. 1976.
- [31] U. F. Kocks, K. UF, A. AS, and A. MF. Thermodynamics and kinetics of slip. 1975.
- [32] A. Koprivica, D. Bajić, N. Šibalić, and M. Vukčević. Analysis of welding of aluminium alloy aa6082-t6 by tig, mig and fsw processes from technological and economic aspect. *Machines. Technologies. Materials.*, 14(5):194–198, 2020.
- [33] J. Langer and k. Schwartz. Kinetics of nucleation in near-critical fluids. *Physical Review A*, 21(3):948, 1980.
- [34] T. Lienert, T. Siewert, S. Babu, and V. Acoff. Factors influencing heat flow in fusion welding. 2011.
- [35] M. Liu, J. Čížek, C. S. Chang, and J. Banhart. Early stages of solute clustering in an al–mg–si alloy. *Acta Materialia*, 91:355–364, 2015.
- [36] D. Lohwasser and Z. Chen. *Friction stir welding: From basics to applications*. Elsevier, 2009.
- [37] C. Marioara, S. Andersen, J. Jansen, and H. Zandbergen. Atomic model for gp-zones in a 6082 al–mg–si system. *Acta Materialia*, 49(2):321–328, 2001.
- [38] C. Marioara, S. Andersen, J. Jansen, and H. Zandbergen. The influence of temperature and storage time at rt on nucleation of the β phase in a 6082 al–mg–si alloy. *Acta Materialia*, 51 (3):789–796, 2003.
- [39] C. D. Marioara, S. Andersen, H. Zandbergen, and R. Holmestad. The influence of alloy composition on precipitates of the al-mg-si system. *Metallurgical and materials transactions A*, 36:691–702, 2005.
- [40] J. Martin. The strength of aged alloys. *Precipitation Hardening*, pages 79–125, 1998.
- [41] G. Mathers. *The welding of aluminium and its alloys*. Elsevier, 2002.
-

-
- [42] K. Matsuda, S. Ikeno, H. Gamada, K. Fujii, Y. Uetani, T. Sato, and A. Kamio. High-resolution electron microscopy on the structure of guinier-preston zones in an al-1.6 mass pct mg 2 si alloy. *Metallurgical and Materials Transactions A*, 29:1161–1167, 1998.
- [43] A. Matsunawa, M. Mizutani, S. Katayama, and N. Seto. Porosity formation mechanism and its prevention in laser welding. *Welding international*, 17(6):431–437, 2003.
- [44] F. M. Mazzolani. *Aluminium structural design*. Number 443. Springer Science & Business Media, 2003.
- [45] H. Mecking and U. Kocks. Kinetics of flow and strain-hardening. *Acta metallurgica*, 29(11):1865–1875, 1981.
- [46] R. S. Mishra and Z. Ma. Friction stir welding and processing. *Materials science and engineering: R: reports*, 50(1-2):1–78, 2005.
- [47] H. Mughrabi, R. W. Cahn, P. Haasen, and E. J. Kramer. *Materials science and technology: a comprehensive treatment*, volume 6. VCH, 1993.
- [48] M. Murayama and K. Hono. Pre-precipitate clusters and precipitation processes in al–mg–si alloys. *Acta materialia*, 47(5):1537–1548, 1999.
- [49] M. Murayama, K. Hono, M. Saga, and M. Kikuchi. Atom probe studies on the early stages of precipitation in al–mg–si alloys. *Materials Science and Engineering: A*, 250(1):127–132, 1998.
- [50] O. Myhr and Ø. Grong. Modelling of non-isothermal transformations in alloys containing a particle distribution. *Acta Materialia*, 48(7):1605–1615, 2000.
- [51] O. Myhr and Ø. Grong. *Asm handbook, welding fundamentals and processes*, 2011.
- [52] O. Myhr, Ø. Grong, and S. Andersen. Modelling of the age hardening behaviour of al–mg–si alloys. *Acta Materialia*, 49(1):65–75, 2001.
- [53] O. Myhr, Ø. Grong, H. Fjær, and C. Marioara. Modelling of the microstructure and strength evolution in al–mg–si alloys during multistage thermal processing. *Acta Materialia*, 52(17):4997–5008, 2004.
- [54] O. R. Myhr, Ø. Grong, and K. O. Pedersen. A combined precipitation, yield strength, and work hardening model for al-mg-si alloys. *Metallurgical and Materials Transactions A*, 41(9):2276–2289, 2010.
- [55] O. R. Myhr, Ø. Grong, and C. Schäfer. An extended age-hardening model for al-mg-si alloys incorporating the room-temperature storage and cold deformation process stages. *Metallurgical and Materials Transactions A*, 46(12):6018–6039, 2015.
- [56] O. R. Myhr, O. S. Hopperstad, and T. Børvik. A combined precipitation, yield stress, and work hardening model for al-mg-si alloys incorporating the effects of strain rate and temperature. *Metallurgical and Materials Transactions A*, 49(8):3592–3609, 2018.
- [57] E. Nes. Recovery revisited. *Acta metallurgica et materialia*, 43(6):2189–2207, 1995.
- [58] E. Nes and K. Marthinsen. Modeling the evolution in microstructure and properties during plastic deformation of fcc-metals and alloys—an approach towards a unified model. *Materials Science and Engineering: A*, 322(1-2):176–193, 2002.
- [59] J. R. Olsen. A combined thermal cycle software for welded and locally heat treated 6082 aluminium alloys. Master’s thesis, NTNU, 2020.
- [60] W. Poole and D. Lloyd. Modelling the stress-strain behaviour for aluminum alloy aa 6111. In *Materials Forum*, volume 28, pages 939–944, 2004.
- [61] W. Poole, H. Shercliff, and T. Castillo. Process model for two step age hardening of 7475 aluminium alloy. *Materials science and technology*, 13(11):897–904, 1997.
- [62] D. Porter. *Ke easterling phase transformations in metals and alloys*, 1992.
-

-
- [63] E. Povoden-Karadeniz, P. Lang, P. Warczok, A. Falahati, W. Jun, and E. Kozeschnik. Calphad modeling of metastable phases in the al–mg–si system. *Calphad*, 43:94–104, 2013. ISSN 0364-5916. doi: <https://doi.org/10.1016/j.calphad.2013.03.004>. URL <https://www.sciencedirect.com/science/article/pii/S0364591613000345>.
- [64] C. Ravi and C. Wolverton. First-principles study of crystal structure and stability of al–mg–si–(cu) precipitates. *Acta materialia*, 52(14):4213–4227, 2004.
- [65] O. Reiso. Extrusion of almg-si alloys. In *Materials Forum*, volume 28, pages 32–46, 2004.
- [66] W. Rethwisch. Callister, materials science and engineering, 2010.
- [67] A. Rusinek and J. Rodríguez-Martínez. Thermo-viscoplastic constitutive relation for aluminium alloys, modeling of negative strain rate sensitivity and viscous drag effects. *Materials & Design*, 30(10):4377–4390, 2009.
- [68] J. Saeter, B. Forbord, H. Vatne, and E. Nes. Proceedings of the 6th international conference on aluminum alloys (icaa6), japan institute of light metals, tokyo. *Japan*, 1:113–126, 01 1998.
- [69] V.-A. Silvestru, I. Ariza, and A. Taras. Structural behaviour of point-by-point wire arc additively manufactured steel bars under compressive loading. *Journal of Constructional Steel Research*, 207:107982, 2023.
- [70] Y. Takaki, Y. Aruga, M. Kozuka, and T. Sato. Effects of pre-aging and natural aging on bake hardening behavior in al–mg–si alloys. In *Materials Science Forum*, volume 794, pages 1026–1031. Trans Tech Publ, 2014.
- [71] K. Teichmann, C. D. Marioara, S. J. Andersen, and K. Marthinsen. The effect of preaging deformation on the precipitation behavior of an al–mg–si alloy. *Metallurgical and Materials Transactions A*, 43(11):4006–4014, 2012.
- [72] K. Teichmann, C. D. Marioara, S. J. Andersen, and K. Marthinsen. Tem study of β precipitate interaction mechanisms with dislocations and β interfaces with the aluminium matrix in al–mg–si alloys. *Materials characterization*, 75:1–7, 2013.
- [73] W. Thomas M., E. Nicholas D., N. James C., M. Michael G., T.-S. Peter, and D. Christopher J. Friction stir welding, United States Patent 5 460 317, Oct. 1995.
- [74] M. Torsæter, W. Lefebvre, S. J. Andersen, C. D. Marioara, J. C. Walmsley, and R. Holmestad. Clustering behaviour in al–mg–si alloys investigated by apt. In *Proceedings of the 12th International Conference on Aluminium Alloys (ICAA12)*, pages 1385–1390, 2010.
- [75] A. H. van den Boogaard and J. Huétink. Simulation of aluminium sheet forming at elevated temperatures. *Computer methods in applied mechanics and engineering*, 195(48-49):6691–6709, 2006.
- [76] V. Vilamosa, A. H. Clausen, T. Børvik, B. Holmedal, and O. S. Hopperstad. A physically-based constitutive model applied to aa6082 aluminium alloy at large strains, high strain rates and elevated temperatures. *Materials & Design*, 103:391–405, 2016.
- [77] R. Vissers, M. v. van Huis, J. Jansen, H. Zandbergen, C. Marioara, and S. Andersen. The crystal structure of the β phase in al–mg–si alloys. *Acta Materialia*, 55(11):3815–3823, 2007.
- [78] R. Wagner and R. Kampmann. *Material Science and Technology-A Comprehensive Treatment*, volume 5. VCH, 1991.
- [79] K. Weman. *Welding processes handbook*. Elsevier, 2011.
- [80] K. Weman and G. Lindén. *MIG welding guide*. Woodhead Publishing, 2006.
- [81] D. Yaduwanshi, S. Bag, and S. Pal. Effect of preheating in hybrid friction stir welding of aluminum alloy. *Journal of materials engineering and performance*, 23(10):3794–3803, 2014.
-

Appendix

A Temperature Measurements During Welding

As can be seen in section 4, a lot of weldings were done in this thesis. The temperature was measured at different distances for all of these, and it seems unnecessary to include all of the temperature measurements as many of them are very similar. Only the measurements from the FSW of the T6-reference alloy (figure 40), the FSW alloy after water cooling (figure 41), the MIG welded alloy after heating to 430°C and cooling in the oven (figure ?? and 42) and the MIG welded alloy after heating to 550°C and air cooling (figure 44 and 45) are included in the appendix. Since two weldings were done for MIG, two figures of the temperature measurement is shown here, describing both the first and second welding. All the figures are given below.

Figure 40: The temperature during FSW of the T6-reference alloy. The temperature was measured at the distances 5mm, 9mm and 13mm from the weld centre, as can be seen in the figure.

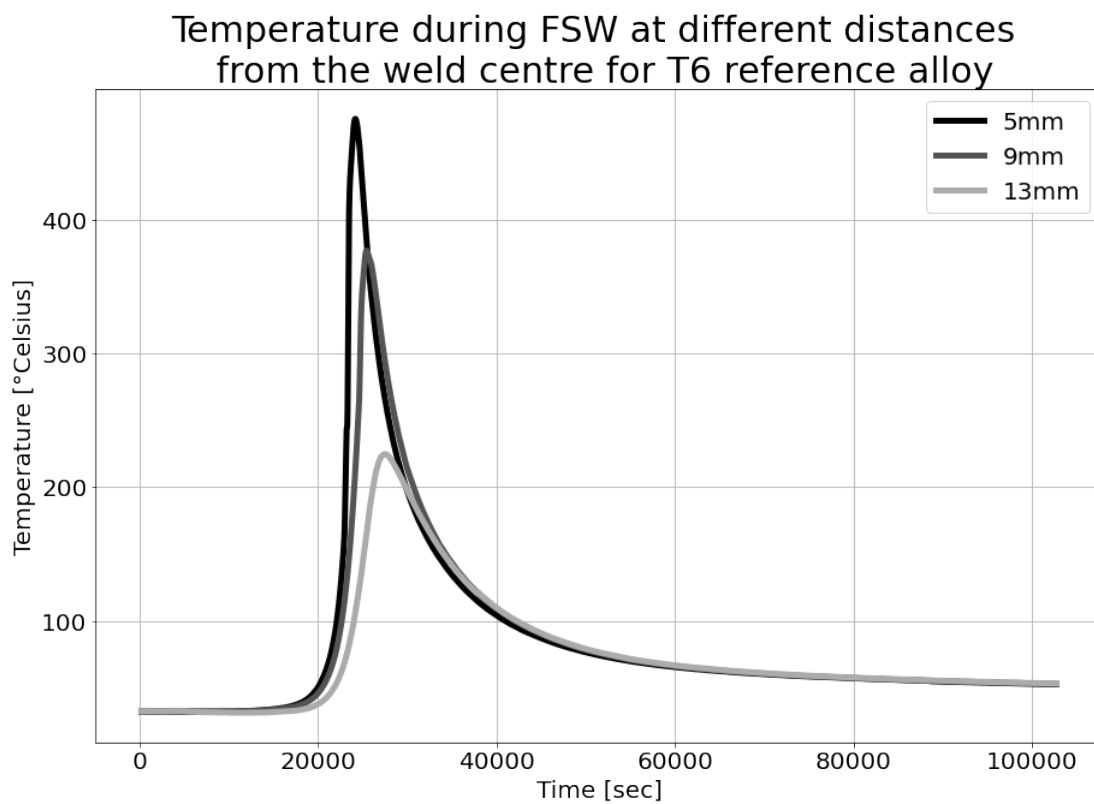


Figure 41: The temperature during FSW of the warm water cooled alloy after heating to 430°C. The temperature was measured at the distances 5mm, 9mm and 13mm from the weld centre, as can be seen in the figure.

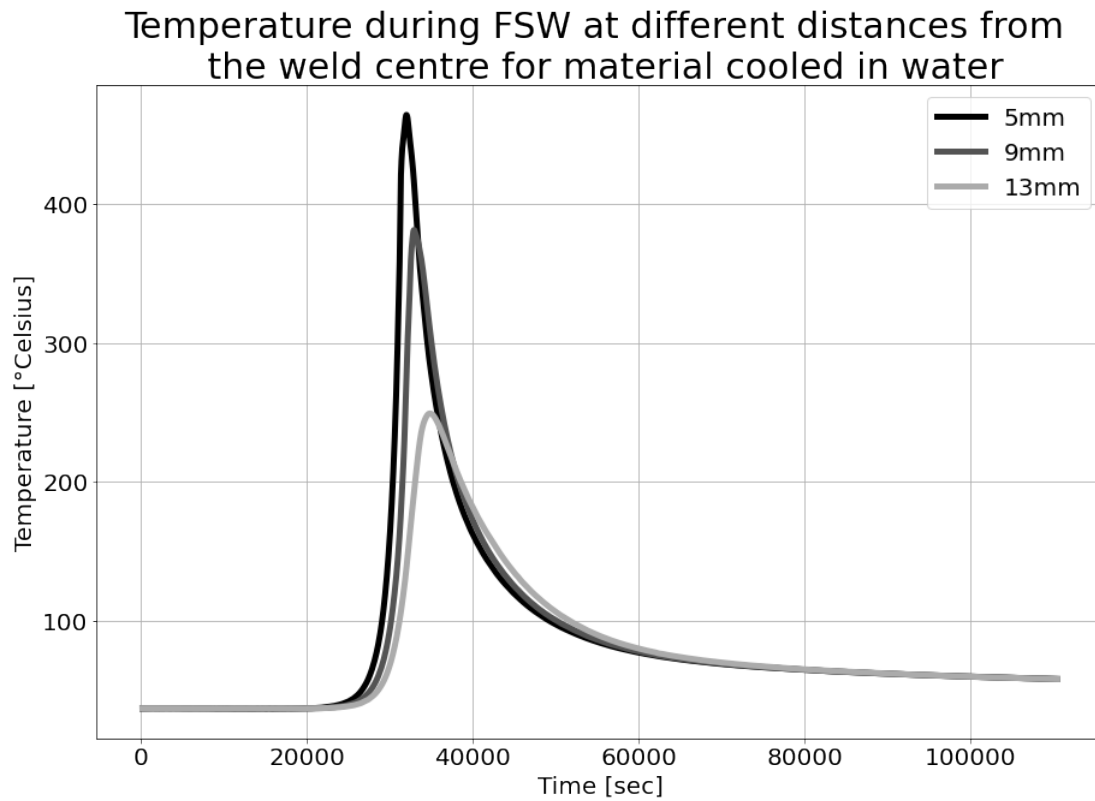


Figure 42: The temperature during MIG welding of the alloy cooled in the oven after heating to 430°C for the first weld. The temperature was measured at the distances 5mm, 9mm and 13mm, 25mm and 75mm from the weld centre, as can be seen in the figure.

Temperature during MIG at different distances
from the weld centre for material cooled
in oven after heating to 430°C during first weld

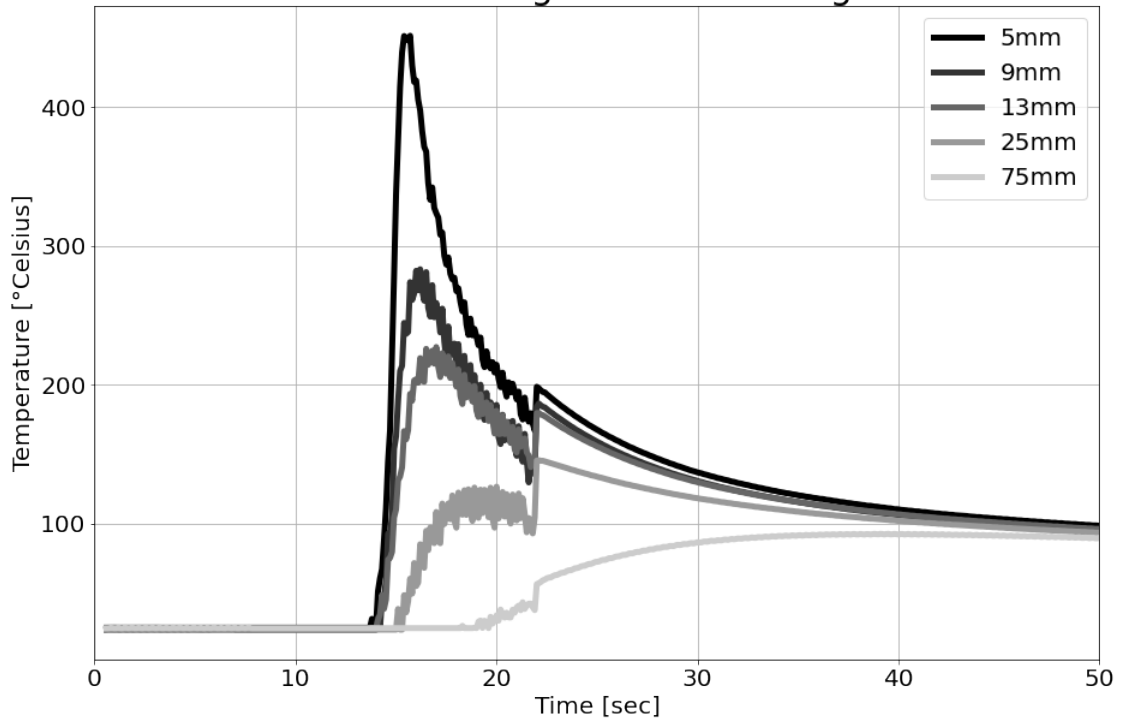


Figure 43: The temperature during MIG welding of the alloy cooled in the oven after heating to 430°C for the second weld. The temperature was measured at the distances 5mm, 9mm and 13mm, 25mm and 75mm from the weld centre, as can be seen in the figure.

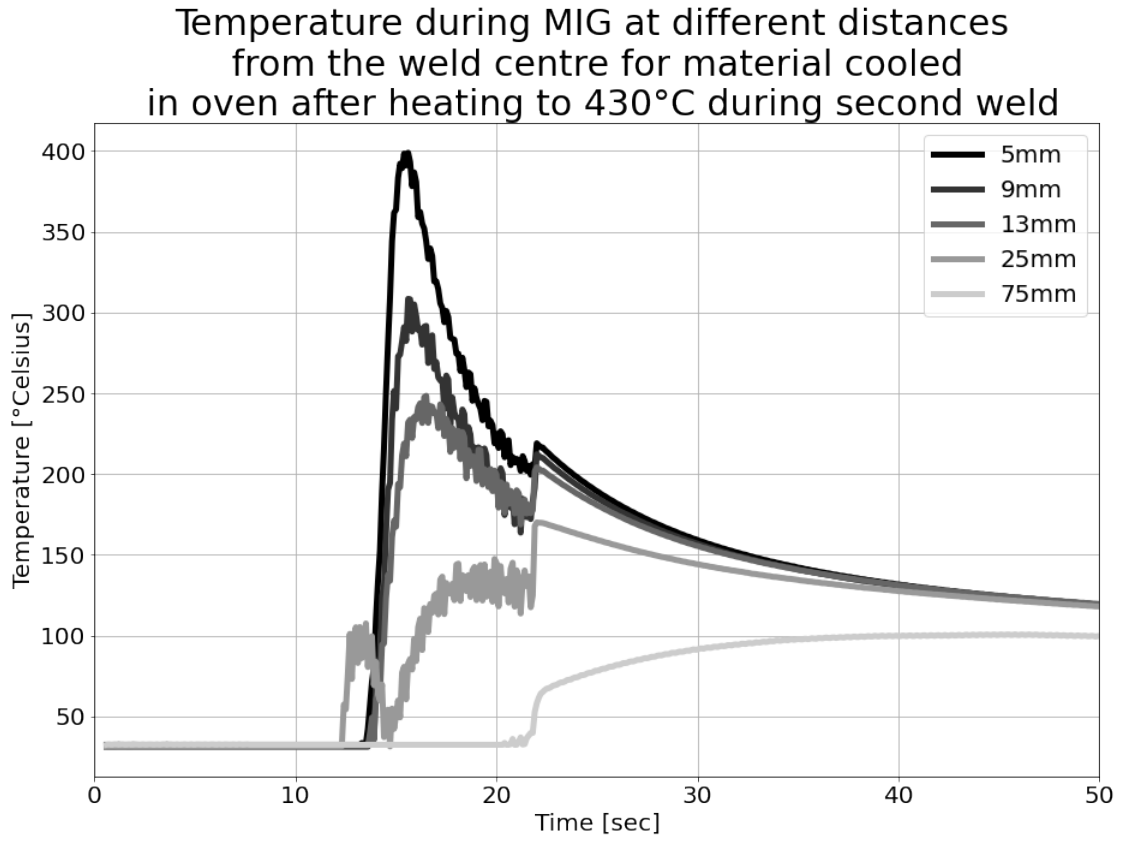


Figure 44: The temperature during MIG welding of the air cooled alloy after heating to 550°C for the first weld. The temperature was measured at the distances 5mm, 9mm and 13mm from the weld centre, as can be seen in the figure.

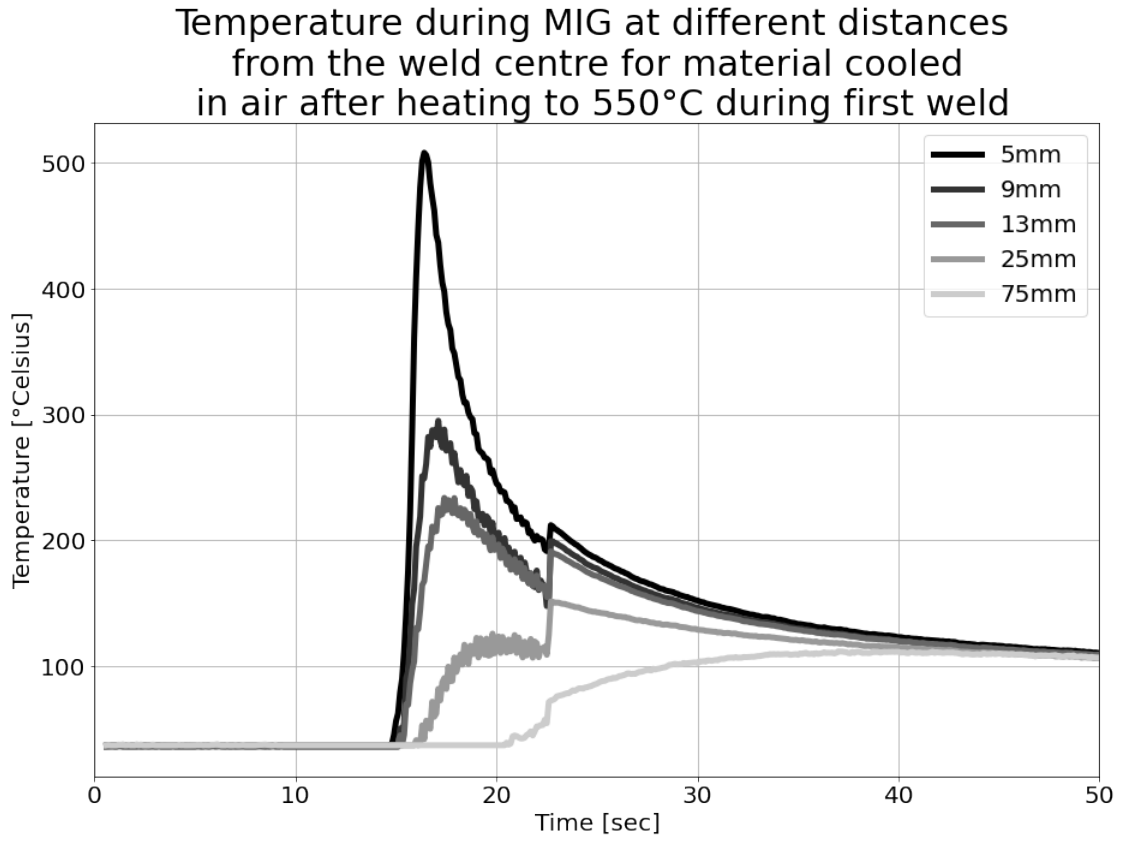
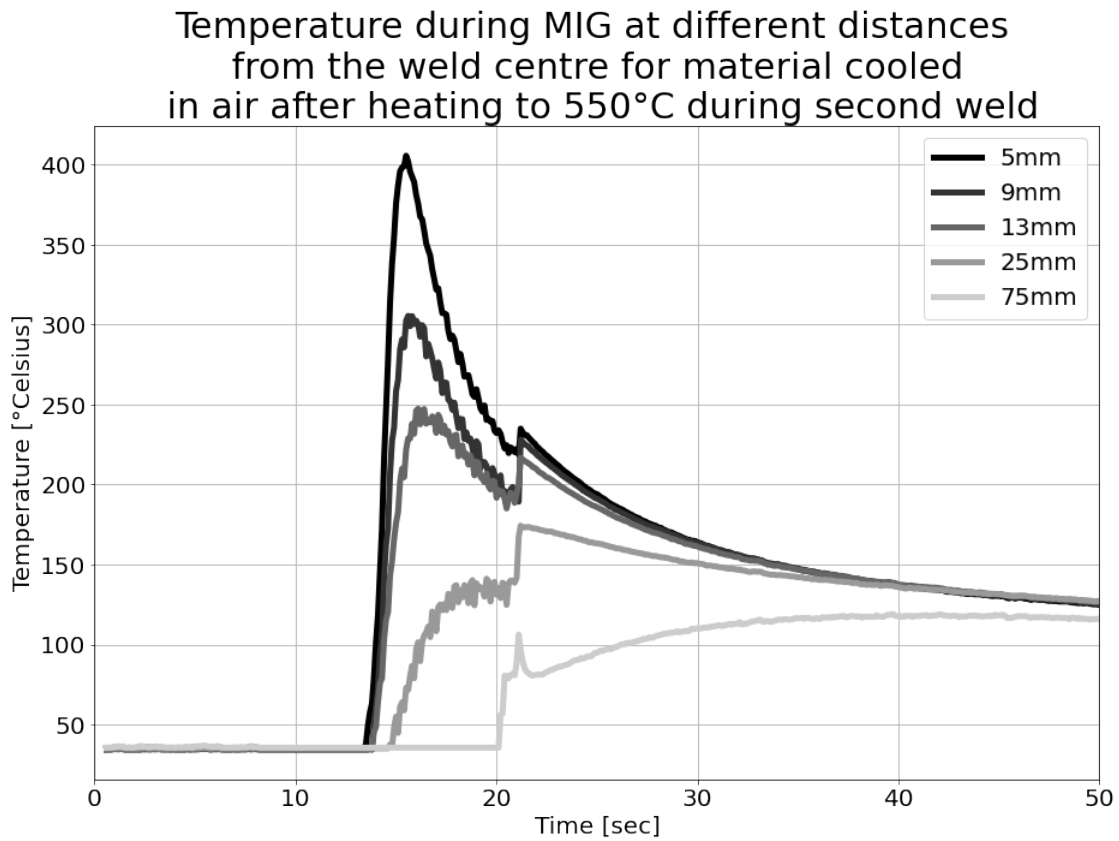


Figure 45: The temperature during MIG welding of the air cooled alloy after heating to 550°C for the second weld. The temperature was measured at the distances 5mm, 9mm and 13mm from the weld centre, as can be seen in the figure.



B Inputs NaMo

Similarly as for the temperature measurements, only a small number of the NaMo simulation inputs are included in this appendix. All the NaMo simulation inputs are from a distance 9mm from the weld centre. The given screenshots of inputs are the same as the given temperature measurements. These are the T6-reference alloy for FSW (figure 46), the FSW alloy after water cooling (figure 47), the MIG welded alloy after heating to 430°C and cooling in the oven (figure 48) and the MIG welded alloy after heating to 550°C and air cooling (figure 49). The figures can be found below.

Figure 46: The input to NaMo at a distance 9mm from the weld centre for the plate in a T6 reference state experiencing FSW.

Alloys		Temperature-Time			
Alloys		T1 (°C)			
0.65	Mg (wt%)	560			
0.9	Si (wt%)	T2 (°C)	Time T1-T2 (s)	# time steps	Plastic strain (%)
0.32	Fe (wt%)	20	35	500	0
0.55	Mn (wt%)	T3 (°C)	Time T2-T3 (s)	# time steps	Plastic strain (%)
0.1	Cu (wt%)	185	60	500	0
0.001	Cr (wt%)	T4 (°C)	Time T3-T4 (s)	# time steps	Plastic strain (%)
		185	18000	500	0
		T5 (°C)	Time T4-T5 (s)	# time steps	Plastic strain (%)
		20	60	500	0
		T6 (°C)	Time T5-T6 (s)	# time steps	Plastic strain (%)
		385	5	500	0
		T7 (°C)	Time T6-T7 (s)	# time steps	Plastic strain (%)
		80	35	500	0
		T8 (°C)	Time T7-T8 (s)	# time steps	Plastic strain (%)
		20	600	500	0
		T9 (°C)	Time T8-T9 (s)	# time steps	Plastic strain (%)
		20	10000	500	0
		T10 (°C)	Time T9-T10 (s)	# time steps	Plastic strain (%)
		185	0	500	0
		T11 (°C)	Time T10-T11 (s)	# time steps	Plastic strain (%)
		185	0	500	0
		T12 (°C)	Time T11-T12 (s)	# time steps	Plastic strain (%)
		185	0	500	0

Figure 47: The input to NaMo at a distance 9mm from the weld centre for the warm water cooled plate experiencing FSW.

Alloys		Temperature-Time			
Alloys		T1 (°C)			
0.65	Mg (wt%)	560			
0.9	Si (wt%)	T2 (°C)	Time T1-T2 (s)	# time steps	Plastic strain (%)
0.32	Fe (wt%)	20	35	500	0
0.55	Mn (wt%)	T3 (°C)	Time T2-T3 (s)	# time steps	Plastic strain (%)
0.1	Cu (wt%)	433	3600	500	0
0.001	Cr (wt%)	T4 (°C)	Time T3-T4 (s)	# time steps	Plastic strain (%)
		433	240	500	0
		T5 (°C)	Time T4-T5 (s)	# time steps	Plastic strain (%)
		89	1	500	0
		T6 (°C)	Time T5-T6 (s)	# time steps	Plastic strain (%)
		55	5043	500	0
		T7 (°C)	Time T6-T7 (s)	# time steps	Plastic strain (%)
		20	120	500	0
		T8 (°C)	Time T7-T8 (s)	# time steps	Plastic strain (%)
		380	5	500	0
		T9 (°C)	Time T8-T9 (s)	# time steps	Plastic strain (%)
		80	50	500	0
		T10 (°C)	Time T9-T10 (s)	# time steps	Plastic strain (%)
		20	600	500	0
		T11 (°C)	Time T10-T11 (s)	# time steps	Plastic strain (%)
		20	10000	500	0
		T12 (°C)	Time T11-T12 (s)	# time steps	Plastic strain (%)
		185	0	500	0

Figure 48: The input to NaMo at a distance 9mm from the weld centre for the plate cooled in the oven experiencing MIG welding after being heated to 430°C.

Alloys		Temperature-Time			
Alloys		T1 (°C)			
0.65	Mg (wt%)	560			
0.9	Si (wt%)	T2 (°C)	Time T1-T2 (s)	# time steps	Plastic strain (%)
0.32	Fe (wt%)	20	35	500	0
0.55	Mn (wt%)	T3 (°C)	Time T2-T3 (s)	# time steps	Plastic strain (%)
0.1	Cu (wt%)	433	3600	500	0
0.001	Cr (wt%)	T4 (°C)	Time T3-T4 (s)	# time steps	Plastic strain (%)
		20	60000	500	0
		T5 (°C)	Time T4-T5 (s)	# time steps	Plastic strain (%)
		280	3	500	0
		T6 (°C)	Time T5-T6 (s)	# time steps	Plastic strain (%)
		100	35	500	0
		T7 (°C)	Time T6-T7 (s)	# time steps	Plastic strain (%)
		20	600	500	0
		T8 (°C)	Time T7-T8 (s)	# time steps	Plastic strain (%)
		305	3	500	0
		T9 (°C)	Time T8-T9 (s)	# time steps	Plastic strain (%)
		100	35	500	0
		T10 (°C)	Time T9-T10 (s)	# time steps	Plastic strain (%)
		20	600	500	0
		T11 (°C)	Time T10-T11 (s)	# time steps	Plastic strain (%)
		20	1000000	500	0
		T12 (°C)	Time T11-T12 (s)	# time steps	Plastic strain (%)
		185	0	500	0

Figure 49: The input to NaMo at a distance 9mm from the weld centre for the air cooled plate experiencing MIG welding after being heated to 550°C.

Alloys		Temperature-Time			
Alloys		T1 (°C)			
0.65	Mg (wt%)	560			
0.9	Si (wt%)	T2 (°C)	Time T1-T2 (s)	# time steps	Plastic strain (%)
0.32	Fe (wt%)	100	900	500	0
0.55	Mn (wt%)	T3 (°C)	Time T2-T3 (s)	# time steps	Plastic strain (%)
0.1	Cu (wt%)	20	3600	500	0
0.001	Cr (wt%)	T4 (°C)	Time T3-T4 (s)	# time steps	Plastic strain (%)
		20	100000	500	0
		T5 (°C)	Time T4-T5 (s)	# time steps	Plastic strain (%)
		300	3	500	0
		T6 (°C)	Time T5-T6 (s)	# time steps	Plastic strain (%)
		100	35	500	0
		T7 (°C)	Time T6-T7 (s)	# time steps	Plastic strain (%)
		20	600	500	0
		T8 (°C)	Time T7-T8 (s)	# time steps	Plastic strain (%)
		300	3	500	0
		T9 (°C)	Time T8-T9 (s)	# time steps	Plastic strain (%)
		100	35	500	0
		T10 (°C)	Time T9-T10 (s)	# time steps	Plastic strain (%)
		20	600	500	0
		T11 (°C)	Time T10-T11 (s)	# time steps	Plastic strain (%)
		20	1000000	500	0
		T12 (°C)	Time T11-T12 (s)	# time steps	Plastic strain (%)
		185	0	500	0

In these figures, it should be noted that the FSW plates has less heating steps than the MIG welded plates. This is because the FSW only included one welding, while the MIG welding needed two weldings, as described in section 3.



 **NTNU**

Norwegian University of
Science and Technology